



Università degli Studi Mediterranea di Reggio Calabria
Archivio Istituzionale dei prodotti della ricerca

The influence of a cyclic loading history on soil-geogrid interaction under pullout condition

This is the peer reviewed version of the following article:

Original

The influence of a cyclic loading history on soil-geogrid interaction under pullout condition / Cardile, Giuseppe; Pisano, M; Moraci, Nicola; Marilene, Pisano. - In: GEOTEXTILES AND GEOMEMBRANES. - ISSN 0266-1144. - 47:4(2019), pp. 552-565. [10.1016/j.geotexmem.2019.01.012]

Availability:

This version is available at: <https://hdl.handle.net/20.500.12318/1337> since: 2021-02-22T18:55:26Z

Published

DOI: <http://doi.org/10.1016/j.geotexmem.2019.01.012>

The final published version is available online at: <https://www.sciencedirect.com>.

Terms of use:

The terms and conditions for the reuse of this version of the manuscript are specified in the publishing policy. For all terms of use and more information see the publisher's website

Publisher copyright

This item was downloaded from IRIS Università Mediterranea di Reggio Calabria (<https://iris.unirc.it/>) When citing, please refer to the published version.

(Article begins on next page)

1 **THE INFLUENCE OF A CYCLIC LOADING HISTORY ON SOIL-GEOGRID**
2 **INTERACTION UNDER PULLOUT CONDITION**

3 G. Cardile¹, M. Pisano² and N. Moraci³

4 1 Assistant Professor of Geotechnical Engineering, Ph.D. — *Mediterranea* University of Reggio
5 Calabria, Department of Civil Engineering, Energy, Environment and Materials (DICEAM), Italy-
6 Telephone: +39 0965 169 2213; Telefax: +39 0965 1692201, e-mail: giuseppe.cardile@unirc.it
7 (corresponding author)

8 2 Research assistant in Geotechnical Engineering, Ph.D. — *Mediterranea* University of Reggio Calabria,
9 Department of Civil Engineering, Energy, Environment and Materials (DICEAM), Italy- Telephone: +39
10 0965 169 2223; Telefax: +39 0965 1692201, e-mail: marilene.pisano@unirc.it

11 3 Full Professor of Geotechnical Engineering, Ph.D. — *Mediterranea* University of Reggio Calabria,
12 Department of Civil Engineering, Energy, Environment and Materials (DICEAM), Italy- Telephone: +39
13 0965 169 2263; Telefax: +39 0965 1692201, e-mail: nicola.moraci@unirc.it

14

15 **ABSTRACT**

16 The knowledge of soil-geosynthetic interface behaviour is a key point in the design of
17 geosynthetic-reinforced soil structures. The pullout ultimate limit state can be
18 reproduced conveniently by means of pullout tests performed with large-size laboratory
19 apparatuses, which allow studying the interaction mechanisms that develop in the
20 anchorage zone. During the service life of geosynthetic-reinforced soil structures,
21 reinforcements may be subjected to long-term cyclic vehicular loads or short-term
22 seismic loads in addition to dead loadings, such as the structure's self-weight and other
23 sustained loads. In order to study the influence of a cyclic loading history (a sinusoidal
24 function with fixed amplitude A , number of cycles N and frequency f) on the post-cyclic
25 peak pullout resistance, the writers carried out a series of multi-stage pullout tests on a
26 high density polyethylene extruded uniaxial geogrid embedded in a compacted granular

27 soil for different vertical effective stress σ'_v values. Moreover, the stability of the soil-
28 geosynthetic interface from a point of view linked to the cyclic loading application has
29 also been investigated. Test results showed that the design pullout resistance parameters
30 are affected by the applied cyclic loading history for specific combined conditions (A , N
31 and σ'_v) and it should be taken into account for designing geosynthetic reinforced soil
32 structures.

33

34 **KEYWORDS:** geosynthetics, geogrid, pullout, cyclic loading, soil-reinforcement
35 interface, multi-stage test, residual strain, design parameters, apparent coefficient of
36 friction, viscous properties.

37 **1 INTRODUCTION**

38 Different approaches can be used to study the seismic behaviour of geosynthetic-
39 reinforced soil (GRS) structures, ranging from empirical observations of damages
40 caused on GRS works by seismic events (Carrubba and Colonna, 2000; Huang et al.,
41 2003; Koseki et al., 2006; Koseki et al., 2009; Ling and Leshchinsky, 2005; Ling et al.,
42 2001; Tatsuoka et al., 1995, 1997; Wartman et al., 2006; White and Holtz, 1994) to the
43 results' interpretation of tests carried out on full-scale or reduced-scale physical models
44 (Capilleri et al., 2019; El-Emam and Bathurst, 2004; El-Emam and Bathurst, 2005;
45 Izawa et al., 2004; Ling et al., 2005; Matsuo et al., 1998; Nova-Roessig and Sitar, 2006;
46 Sabermahani et al., 2009; Watanabe et al., 2003), up to theoretical studies such as
47 *pseudo-static analyses* (Bathurst and Cai, 1995; Biondi et al., 2013; Michalowski, 1998;
48 Motta, 1996; Nouri et al., 2006), *seismic displacement analyses* (Ausilio et al., 2000;
49 Cai and Bathurst, 1996a, b; Di Filippo et al., 2019; Gaudio et al., 2018; Ling et al.,

50 1997; Michalowski and You, 2000; Paulsen and Kramer, 2004) and *dynamic numerical*
51 *methods* (Hatami and Bathurst, 2000; Lee et al., 2010; Ling et al., 2004).

52 One of the parameters necessary to design GRS works by using the pseudo-static
53 approach is the apparent coefficient of friction between soil and geosynthetic, which
54 allows determining the reinforcement length and consequently the reinforced block size
55 (Abramento, 1995; Carbone et al., 2015; Jewell, 1990; Leshchinsky, 2009; Leshchinsky
56 et al., 2014; Leshchinsky et al., 1995; Moraci and Cardile, 2008; Moraci et al., 2014;
57 Moraci and Recalcati, 2006; Pavanello et al., 2018).

58 The seismic displacement analyses are performance-based approaches that originate
59 from the Newmark's sliding block method (Newmark, 1965), assuming that the soil
60 mass moves as a rigid block along a potential sliding surface, with permanent
61 displacements occurring when the forces acting on it exceed the available shear
62 resistance. Whenever the ground acceleration overcomes the critical acceleration, the
63 rigid block's permanent displacement increases and it can be considered as a measure of
64 the possible damage caused by an earthquake. The friction interaction coefficient
65 between soil and reinforcement is required also in these cases.

66 The dynamic analysis uses numerical methods such as finite element, finite difference
67 and coupled finite element-discrete element methods, which need as input constitutive
68 models capable to reproduce the stress-strain relationships for soil, geosynthetics and
69 soil-reinforcement interfaces in the best way possible so as to provide accurate results.

70 Therefore, comprehension of the soil-geosynthetic interface behaviour is extremely
71 important whichever seismic method is chosen to design GRS structures. For this
72 purpose, it is necessary to analyse the soil-geosynthetic interaction in terms of pullout
73 resistance and displacement behaviour by using pullout tests under cyclic loading

74 conditions as the more suitable tool. As things stand, few researches studied these
75 aspects on different geosynthetics-granular soil interfaces generally subject to cyclic
76 loading at frequencies up to 0.5 Hz (Min et al., 1995; Moraci and Cardile, 2009, 2012;
77 Nayeri and Fakharian, 2009; Nernheim, 2005; Raju and Fannin, 1997; Razzazan et al.,
78 2018; Yasuda et al., 1992). In this context, the paper aims to expand knowledge of the
79 cyclic and post-cyclic pullout behaviour of a high density polyethylene (HDPE)
80 extruded uniaxial geogrid embedded in a compacted granular soil subject to cyclic
81 pullout loading with a higher frequency ($f=1$ Hz), more representative of long-term
82 vehicular loads or short-term seismic loads, varying the cyclic load amplitude and the
83 vertical effective stress. To take into account cyclic or dynamic loads potentially acting
84 on GRS structures' reinforcements in addition to sustained loadings, the pullout tests
85 were carried out using a multi-stage procedure. The influences of cyclic tensile loading
86 amplitude A , number of cycles N and vertical effective stress σ'_v on the parameters
87 obtained during hysteresis loops have been analysed in depth. Moreover, the difference
88 between post-cyclic and static peak pullout resistances has also been investigated by
89 comparing pullout curves for the multi-stage tests and those for the corresponding tests
90 at constant rate of displacement.

91 **2 EXPERIMENTAL STUDY**

92 **2.1 Apparatus**

93 The test apparatus used in the research (Cardile et al., 2016a; Moraci and Recalcati,
94 2006) consists of different components (Figure 1a, b, c):

95 i) a pullout steel box having large dimensions (1700x600x680 mm) and walls covered
96 with Teflon films to avoid friction effects;

97 ii) a rubber flexible membrane filled with air for the application of vertical loads;
98 iii) a hydraulic actuator for displacement- or load-controlled pullout testing for the
99 application of horizontal loads;
100 iv) a clamping system inside the box to maintain the reinforcement specimen always
101 confined for the whole duration of the test;
102 v) a pair of metal sleeves at the front wall to avoid its stiffness effects on results;
103 vi) a load cell for measuring the pullout force; and
104 vii) six linear variable displacement transducers (LVDT) connected to six different
105 points of the reinforcement's specimen by means of inextensible steel wires to measure
106 the specimen's displacements.
107 Unlike the apparatus used in previous researches, the new actuator is able to simulate
108 pullout cyclic loadings that can reach high frequencies (up to 4 Hz).

109 **2.2 Test materials**

110 The soil used in this research is a uniform medium sand classified as SP and A-3
111 according to USCS (ASTM D2487, 2017) and UNI EN ISO 14688-1 (2018)
112 classification systems respectively, with grain shape ranging from sub-rounded to
113 rounded, uniformity coefficient (U) equal to 1.96, and average grain size (D_{50}) equal to
114 0.32 mm. The compaction of soil inside the pullout box was carried out until reaching a
115 dry unit weight value equal to 95% of the maximum dry unit weight ($\gamma_{dmax} = 16.24$
116 kN/m^3 , at an optimum water content $w_{opt} = 13.5\%$) obtained by AASHTO T 99 (2015)
117 Standard Proctor compaction tests (ASTM D698-12e2, 2012; UNI EN ISO 13286-2,
118 2010). Direct shear tests, performed at $\gamma_d = 95\% \gamma_{dmax}$, yielded values of the soil peak
119 shear-strength angle ϕ'_P from 48° (for $\sigma'_v = 10 \text{ kPa}$) to 42° (for $\sigma'_v = 100 \text{ kPa}$). The soil

120 shear-strength angle at constant volume ϕ'_{CV} was equal to 34° (Moraci and Recalcati,
121 2006).
122 The geosynthetic used in the pullout tests is an HDPE uniaxial extruded geogrid. Its
123 mechanical behaviour was investigated by means of wide-width tensile tests (Cardile et
124 al., 2016b; Cardile et al., 2017b) in the standard atmosphere for testing ($20\pm 2^\circ\text{C}$ at
125 $65\pm 5\%$ RH) at constant strain rate (CSR) equal to 20% per minute, using index test
126 procedures (ISO 10319:2015). Additional tensile tests at CSR equal to $\dot{\epsilon}'=0.2\%$ per
127 minute were also carried out to make comparison with the rate used in pullout tests
128 carried out at constant rate of displacement. Table 1 lists the tensile test results at
129 constant strain rates equal to 20% and 0.2% per minute.

130 **2.3 Test procedure**

131 The multi-stage pullout tests were performed on geogrid specimens 1.20 m long, at
132 different vertical effective stresses ($\sigma'_v = 10, 25, 50, 100$ kPa), by using a multi-stage
133 procedure (MS) consisting of three steps (Moraci and Cardile, 2009, 2012):
134 • a displacement-controlled stage at constant rate of displacement (CRD) equal to 1 mm
135 per minute, reaching a fixed pullout load P_i ;
136 • a load-controlled cyclic stage using a sinusoidal function, with a fixed tensile loading
137 amplitude A and frequency $f=1$ Hz, for $N=1000$ cycles in total;
138 • a post-cyclic stage that is a displacement-controlled stage at $\text{CRD}=1$ mm per minute
139 once again, until a maximum horizontal displacement equal to 100 mm, the specimen
140 pullout or its rupture was reached.
141 Both P_i and A were chosen as a percentage of P_R that is the peak pullout resistance (per
142 unit width) obtained by pullout tests under static conditions, carried out at the same
143 confining pressure and $\text{CRD}=1$ mm per min. Specifically, $P_i \approx 35\% P_R$ was adopted for

144 the first one since it could be considered as an upper bound value (taking into account
145 surcharge, geometry, partial coefficients to be used for the reduction of the interface
146 parameters according to several international recommendations, etc.) for those
147 representative of GRS structures' design. Moreover, in order to investigate the influence
148 in changing the cyclic loading amplitude, two different A values ($A \approx 30\% P_R$ and
149 $A \approx 45\% P_R$) were chosen for the maximum loading level falling into the range between
150 P_i and P_R .

151 Table 2 lists the MS pullout test program, highlighting that the actually-made cycles
152 were lower than the planned ones for the higher applied amplitude ($A \approx 45\% P_R$) at
153 $\sigma'_v < 100$ kPa due to the achievement of the clamp maximum displacement allowed by
154 this apparatus.

155 **3 ANALYSIS OF TEST RESULTS**

156 **3.1 Cyclic stability of soil-geogrid interface**

157 Accumulation of permanent strains, which occurs cycle by cycle under application of
158 non-zero mean tensile stress (ratcheting), is observed on both soil and geosynthetics
159 when a cyclic load is applied (Alonso-Marroquín and Herrmann, 2004; Calvetti and di
160 Prisco, 2010; Cardile et al., 2016b; Cardile et al., 2017b; Kongkitkul et al., 2004; Ling
161 et al., 1998; Vieira and Lopes, 2013). Likewise wide-width cyclic tensile tests, the
162 application of cyclic pullout loads involves the development of hysteresis loops during
163 the cyclic stage.

164 A cyclically stable behaviour of the polymeric reinforcement obtained by means of
165 wide-width cyclic tensile tests (that is, increments of residual strain decrease with
166 increasing number of loading cycles, Cardile et. al, 2017b) is not sufficient to assure a

167 cyclically stable pullout behaviour of the interface soil-reinforcement since the cyclic
 168 loading entails geogrid's deformation as well as its pullout from the soil.
 169 In order to analyse these points, the parameters obtained for each load–unload cycle are
 170 listed separately depending on the reference plane. Specifically, with regard to the P - δ
 171 plane (pullout load versus displacement of the first confined section of specimen) they
 172 are (Figure 2a):

173 • Cyclic displacement's increment measured at the first confined section of
 174 specimen (the specimen head attached to the clamp) and reached during each
 175 cyclic loading, $\Delta\delta_{part,i}^h$;

176 • Cumulative cyclic displacement of the specimen's first confined section,
 177 $\Delta\delta_i^h = \sum_{i=1}^N \Delta\delta_{part,i}^h$;

178 • Cyclic displacement's increment measured at the rear end of the
 179 specimen (the last transverse rib) and reached during each cyclic loading,
 180 $\Delta\delta_{part,i}^e$;

181 • Cumulative cyclic displacement of the specimen's rear end,
 182 $\Delta\delta_i^e = \sum_{i=1}^N \Delta\delta_{part,i}^e$.

183 Regarding the P - ε plane (pullout load versus pullout average strain), the parameters
 184 obtained are (Figure 2b):

185 • Residual strains caused by cyclic loading, ε_r , i.e. when the cyclic loading
 186 returns to the value of the fixed pullout load P_i .

187 For each of these parameters, the influence of tensile loading amplitude A , number of
 188 cycles N and vertical effective stress σ'_v has been investigated.

189 In order to analyse the behaviour at the soil-reinforcement interface, the conceptual
190 model proposed by Moraci and Cardile (2012) has been used by applying a double-
191 graph that shows the relationship between the number of cycles N and $\Delta\delta^h$ on the top
192 part, and between $\Delta\delta^e$ and $\Delta\delta^h$ on the bottom one (Figure 3, Figure 4 and Figure 5).
193 The graphic representations on the top part (Figure 3a, Figure 4a and Figure 5a) allow
194 understanding when the behaviour of soil-reinforcement interface is stable/unstable
195 from a point of view linked to the cyclic loadings application. For a fixed cyclic load
196 history, the cumulative cyclic displacement of the specimen's first confined section is
197 connected both to the residual strains of the geogrid, which occur cycle by cycle under
198 application of cyclic pullout stress, and to the progressive mobilisation of the interaction
199 mechanisms along the specimen that could induce pullout failure.

200 The writers define that the soil-reinforcement interface is cyclically stable when a
201 progressive stabilisation of the interface response is observed. Specifically, this means
202 that the curve $N - \Delta\delta^h$ is concave upward and the cyclic displacement's increments
203 $\Delta\delta_{part,i}^h$ decrease with increasing numbers of cycles: the displacement accumulation rate
204 decreases with increasing N . Nevertheless, it is important to observe that such a
205 cyclically stable condition could be engineeringly unacceptable if the cumulative
206 displacements during the cyclic stage are larger than the allowable displacement for the
207 serviceability limit state.

208 On the contrary, the soil-geogrid interface cyclic behaviour is cyclically unstable when
209 the cyclic displacement's increments $\Delta\delta_{part,i}^h$ become constant or start to increase with
210 increasing numbers of cycles. In the last case, the curve $N - \Delta\delta^h$ has an inflection point
211 becoming concave downward that is, the displacement accumulation rate increases with
212 increasing N , potentially precipitating the achievement of the reinforcement's limit state

213 of failure due to insufficient interaction resistance under pullout conditions between soil
214 and the reinforcement.

215 Regarding graphics on the bottom part (Figure 3b, Figure 4b and Figure 5b), they allow
216 defining more in detail when the soil-geogrid interface approaches the critical condition
217 of pullout failure during the cyclic phase, or rather when the reinforcement is in the:

- 218 • i) load transfer phase. During this phase the active length, that is the portion of
219 the geogrid specimen on which the mobilisation of interaction mechanisms
220 withstands the applied load (Cardile et al., 2016a), increases with the pullout
221 force until this force reaches a limit value that causes the movement of the last
222 transversal bar;
- 223 • ii) pullout phase. During this phase the rear end of the geogrid begins to move
224 and the active length coincides with the entire length of the specimen plus its
225 elongation;
- 226 • iii) pullout limit state. This condition happens when the displacement
227 increments of all specimen points are the same (geogrid stops to deform).

228 Specifically, the reinforcement is in the load transfer phase when the curve $\Delta\delta^e - \Delta\delta^h$
229 evolves in parallel along the $\Delta\delta^h$ x-axis for all cycles since the specimen's rear end is
230 immobile. On the contrary, the reinforcement is in the pullout phase when the curve
231 evolves inside the $\Delta\delta^e - \Delta\delta^h$ admissible area with cyclic displacement's increments of
232 the specimen's rear end that are lower than the corresponding cyclic displacement's
233 increment of the specimen's first confined section for all cycles. Finally, the
234 reinforcement is in the pullout limit state when the curve $\Delta\delta^e - \Delta\delta^h$ becomes parallel
235 with the boundary line between the admissible and inadmissible areas (the

236 displacement's increment of geogrid's head is equal to the displacement's increment
237 measured at the rear end for all the next cycles).

238 **3.1.1 Effect of cyclic loading amplitude**

239 In order to study the influence of loading amplitude A , the double-graph results of MS
240 pullout tests carried out with two different loading amplitudes ($A \approx 30\% P_R$, $45\% P_R$) at
241 the equal value of $P_i \approx 35\% P_R$ are plotted in Figure 3a,b and Figure 4a,b for
242 $\sigma'_v = 50$ kPa and $\sigma'_v = 100$ kPa respectively; the results are representative of all the
243 cases observed in the research.

244 In Figure 3a ($\sigma'_v = 50$ kPa), when $A \approx 30\% P_R$ it is possible to observe a cyclically
245 stable behaviour of the soil-reinforcement interface during all the cyclic stage since the
246 displacement accumulation rate decreases with increasing numbers of cycles. Referring
247 to the results obtained with $A \approx 45\% P_R$, a cyclically unstable behaviour can be
248 observed since there is an inflection point after a certain number of cycles and $\Delta\delta_{part,i}^h$
249 starts to increase with increasing N (the displacement accumulation rate increases). With
250 regard to the pullout condition, Figure 3b shows that when $A \approx 30\% P_R$ the $\Delta\delta^e - \Delta\delta^h$
251 curve evolves inside the admissible area but not in parallel with the boundary line (that
252 is, the cyclic displacement's increment measured at the rear end is lower than the cyclic
253 displacement's increment of the geogrid's head for all cycles), entailing that even the
254 last transversal rib moved; therefore, the geogrid reached the pullout phase. Instead,
255 when $A \approx 45\% P_R$, an unstable pullout behaviour arises as the $\Delta\delta^e - \Delta\delta^h$ curve
256 becomes parallel with the boundary line after a certain number of cycles and pullout
257 failure occurs ($\Delta\delta_{part}^e = \Delta\delta_{part}^h$).

258 For soil-geogrid interface tested at $\sigma'_v = 100$ kPa, a cyclically stable behaviour is
259 noticed for both cyclic amplitudes (Figure 4a); specifically, $\Delta\delta^h$ tends to settle towards

260 a constant value with increasing numbers of cycles. Instead, the behaviour in terms of
261 pullout condition is different, in fact while the geogrid is in the pullout phase when
262 $A \approx 45\% P_R$, it is still in the load transfer phase when $A \approx 30\% P_R$ (Figure 4b) since the
263 curve evolves in parallel along the $\Delta\delta^h$ x-axis for all cycles ($\Delta\delta^e = 0$).
264 Therefore, with regard to the loading amplitude influence it is possible to state that, N
265 being equal, the slope of $N - \Delta\delta^h$ decreases with increasing loading amplitude: for
266 cyclically stable interfaces, the ideal condition of $\Delta\delta^h$ being constant (the displacement
267 accumulation rate is null) is reached for a number of cycles gradually decreasing with
268 decreasing applied loading amplitude, while for cyclically unstable interfaces it is
269 reasonable to expect that the number of cycles at which the displacement accumulation
270 rate becomes constant, or a change in the direction of curvature occurs, decreases with
271 increasing loading amplitude. In other words, the cyclic pullout behaviour of the soil-
272 geogrid interface starts getting worse with increasing cyclic loading amplitude.

273 **3.1.2 The role of vertical effective stresses**

274 To evaluate the influence of the vertical effective stress σ'_v applied to the soil-geogrid
275 interface, the strain behaviour has been investigated analysing MS pullout tests carried
276 out with loading amplitude $A \approx 45\% P_R$ (the MS pullout tests at $A \approx 30\% P_R$ are omitted
277 as they showed a similar behaviour). By observing the top part of Figure 5, the only
278 cyclically stable behaviour is obtained for $\sigma'_v = 100$ kPa. For all the other vertical
279 effective stresses applied, when the inflection point arises the cyclic displacement's
280 increment of the specimen's head starts to increase until pullout failure.
281 On the bottom part of Figure 5 the relationship between the cumulative cyclic
282 displacements of the specimen's first confined section, $\Delta\delta^h$, and the cumulative cyclic
283 displacements of the specimen's rear end, $\Delta\delta^e$, shows an unstable behaviour in terms of

284 pullout condition for $\sigma'_v = 10, 25$ and 50 kPa since their representative curves become
285 parallel with the boundary line between the admissible and inadmissible areas for a
286 number of cycles that increases with increasing σ'_v . When $\sigma'_v = 100$ kPa the interface is
287 still in the pullout phase. Therefore, it is possible to observe that the increase of the
288 vertical effective stress σ'_v plays a clear stabilising role.

289 **3.2 Residual strains and comparison with in-air results**

290 Another important parameter to study the cyclic strain behaviour of the soil-
291 geosynthetic interface is the residual strain ε_r , defined as the cumulative deformation
292 mobilised in the specimen at the end of each corresponding cycle (when the cyclic
293 loading returns to P_i), in agreement with Figure 2b. This parameter allows taking into
294 account the confined stiffness of the geogrid, which exhibits a different response
295 depending on geogrid's geometry, soil type, initial stress state and cyclic loading
296 history.

297 The influence of the vertical effective stress and cyclic loading amplitude is showed in
298 Figure 6a, where the residual strain (evaluated for the entire length of the geogrid, i.e.
299 *apparent strain*) reached at $N = 10$ is plotted versus the vertical effective stress for tests
300 performed at $A \approx 30\% P_R$ and $A \approx 45\% P_R$. The results highlight that the residual strain
301 increases non-linearly with increasing vertical effective stress and, σ'_v being equal, it
302 increases with increasing loading amplitude. The choice to plot the residual strains at
303 cycle $N = 10$ is because tests with $A \approx 45\% P_R$ do not complete all cycles since pullout
304 occurred and the clamp reached the maximum displacement allowed by the apparatus,
305 as it can be observed in Figure 6b. The latter graph displays the residual strain ε_r for
306 varying numbers of cycles on a logarithmic scale, for tests carried out with loading
307 amplitude $A \approx 45\% P_R$ at different vertical effective stress values. It is possible to

308 observe that the residual strain ε_r increases with increasing numbers of cycles and, N
309 being equal, increases with increasing vertical effective stress. Moreover, the number of
310 cycles where the interface exhibits an instable behaviour decreases with decreasing σ'_v
311 ($N = 158, 148, 20$ for $\sigma'_v = 50, 25, 10$ kPa respectively).

312 Kongkitkul et al. (2004) stated that, for the geosynthetic reinforcement types examined
313 by them (such as the HDPE geogrids of this research), the residual strain developed
314 during a certain cyclic loading history is basically due to the loading rate effects caused
315 by the intrinsic viscous properties of the material (therefore, it is controlled by the total
316 period of cyclic loading). The nature of this residual strain is essentially the same as for
317 creep strain developing under an equivalent sustained load. The current research allows
318 studying how the soil confinement affects geogrids strain. Figure 6b points out that for
319 σ'_v ranging from 10 to 50 kPa the $\varepsilon_r - N$ curve deviates from linearity in the semi-
320 logarithmic graph: the strain accumulation rate starts to increase in correspondence with
321 a certain number of cycles that increases with increasing vertical effective stress,
322 highlighting viscous effects similar to the “tertiary creep” phenomenon observed in
323 tensile creep tests, that imply a possible tensile rupture of the reinforcement in case
324 pullout failure does not occur first, such as in this research. Instead, when $\sigma'_v = 100$ kPa
325 the change in ε_r trend is missing since the soil confinement employs a positive effect
326 (Bathurst et al., 2004; Carrubba et al., 2000; Franca and Bueno, 2011; Kongkitkul et al.,
327 2007a, b; Tatsuoka, 2008) increasing the range of numbers of cycles where the strain
328 accumulation rate remains constant (as for the secondary creep phase under sustained
329 tensile loads).

330 Afterwards, by considering the soil-geogrid interface tested at $\sigma'_v = 100$ kPa and
331 $A \approx 30\% P_R, 45\% P_R$ for which a progressive stabilisation of the interface response has

332 been observed, a comparison between their results and those obtained by wide-width
333 tensile multi-stage tests (Cardile et al., 2017b) has been made. In-air tensile tests
334 procedure was similar to the pullout one, with three different stages (two displacement-
335 controlled tensile stages separated by one load-controlled cyclic stage) at the same test
336 conditions (in terms of rate of displacement, P_i , A , N and f). It is more proper to analyse
337 residual strains taking into account the progressive failure mechanisms related to the
338 extensibility of the reinforcement under soil confinement; as a matter of fact, by
339 evaluating individually the residual strains of geogrid's different sections (from a
340 transversal rib to another), the results change remarkably. Figure 7 shows the residual
341 strains evaluated in the cyclic phase of the MS pullout tests for (i) the entire length of
342 the geogrid (residual apparent strains), and (ii) the geogrid's monitored portion closer to
343 its head for varying number of loading cycles at $\sigma'_v = 100$ kPa, $A \approx 30\% P_R$ (Figure 7a)
344 and $\sigma'_v = 100$ kPa, $A \approx 45\% P_R$ (Figure 7b), and the comparison with the corresponding
345 wide-width MS tensile test (Cardile et al., 2017b). This comparison is possible only
346 because the high soil confinement (100 kPa) is preventing the pullout failure, allowing
347 the increase of the applied tensile load. The tensile load applied at the geogrid's head
348 decreases along the specimen until it becomes null (the interaction mechanisms are
349 progressively mobilised on the active length).

350 The shape of the distribution curve representing the tensile stresses along the interface
351 can be very complex, depending on: (i) boundary conditions, (ii) soil mechanical
352 characteristics, and (iii) structural, geometrical and mechanical characteristics of the
353 reinforcement (Bathurst and Ezzein, 2017; Cardile et al., 2014; Cardile et al., 2016a;
354 Moraci et al., 2017; Rahmaninezhad et al., 2019; Roodi and Zornberg, 2017; Wang et
355 al., 2016). Simplifying the stress curve with a triangular distribution, a comparison

356 between the in-air residual strain and the pullout residual strain evaluated for the
357 geogrid's monitored portion closer to its head can be made, as for the latter the load
358 acting on this portion is comparable with the one acting on the entire geogrid in the
359 wide-width MS tensile test (that is, the trapezoidal distribution of tensile stresses along
360 the analysed portion is comparable to a rectangular distribution with a value slightly
361 lower than the in-air one). In particular, this comparison highlights that the geogrid's
362 head strains are much higher than those obtained by in-air multi-stage tensile tests, with
363 increments at $N = 1$ and $N = 1000$ ranging from 305% to 107% for $A \approx 30\%$ P_R (Figure
364 7a) and from 258% to 84% for $A \approx 45\%$ P_R (Figure 7b) respectively. Since the load is
365 similar, this result is probably ascribable to the average test rate of pullout MS tests
366 being lower due to the soil confinement. In fact, while in the in-air tests the average test
367 rate of MS phase is almost the same for the all the points of the extensible specimen, in
368 the pullout tests the rate of MS phase decreases from the head to the free rear end due to
369 the soil confinement; therefore, this lower average test rate causes higher residual
370 strains, owing to the HDPE viscous behaviour. In the same graph, the pullout apparent
371 strains evaluated for the entire length of the geogrid are also plotted; at these conditions,
372 under the simplifying hypothesis of a triangular distribution the load acting on the
373 specimen on average is equal to a half of the load applied to the geogrid's head, acting
374 constantly along the specimen. Since both graphs (Figure 7a,b) show that the apparent
375 residual strain values are similar to those obtained by in-air MS tensile tests, it is
376 possible to state that the effects of the reduction in loading application rate during the
377 confined tests (which entail higher strains) compensate for the effects of decrease in
378 loading acting on average (which, by contrast, entail lower strains).

379 3.3 Effect of cyclic loading history on pullout resistance

380 The influence of cyclic loading history on the pullout behaviour has also been
381 investigated by comparing the pullout curves for the MS tests and those for the
382 corresponding CRD tests. The comparison is reported in Figure 8a,b for the MS pullout
383 tests at $\sigma'_v = 50$ kPa, with loading amplitudes equal to $A \approx 30\% P_R$ and $A \approx 45\% P_R$
384 respectively; these tests are qualitatively representative of all those performed. The
385 pullout forces have been obtained subtracting, at the same displacement value, those
386 from tests carried out without the geogrid in order to eliminate the soil-clamp friction.
387 While in the test performed at $A \approx 45\% P_R$ and $\sigma'_v = 50$ kPa the geogrid has achieved
388 the total horizontal displacement (100 mm) when $N = 158$ (Figure 8b), ergo the post-
389 cyclic stage being not allowed, in the test at $A \approx 30\% P_R$ and $\sigma'_v = 50$ kPa the soil-
390 geogrid interface exhibits a cyclically stable behaviour, although it provides pullout
391 resistance values that are lower than those obtained in the CRD test carried out at the
392 same test condition (Figure 8a). Moreover, by observing the MS curve of Figure 8a it is
393 possible to highlight that the soil-geogrid interface still exhibits a very high tangent
394 stiffness when the post-cyclic stage starts, despite its test rate is lower than the one of
395 cyclic stage, where it is considerably higher on average in order to ensure the intended
396 loading amplitude. After that, the soil-geogrid interface stiffness decreases up to the
397 values obtained for the same displacement in the corresponding CRD pullout test.
398 Therefore, the interface exhibited a yielding phase, in agreement with the results of
399 Hirakawa et al. (2003) for geosynthetics tested in-air.

400 Afterwards, the remaining comparisons for all the vertical effective stresses investigated
401 have been expressed in terms of post-cyclic peak pullout resistance P_R^{PC} (interface's
402 peak pullout resistance obtained in the MS third stage). Figure 9a illustrates P_R^{PC} values

403 obtained in all MS tests with $A \approx 30\%$ P_R normalised with respect to P_R , for varying the
404 vertical effective stress. These results suggest that cyclic loading histories induce a
405 reduction in peak pullout resistance that increases with decreasing vertical effective
406 stresses. For these specific test conditions, the post-cyclic peak pullout resistance
407 reaches decreases up to about 28% compared to the values obtained in monotonic
408 pullout tests at the same test conditions. The higher decrease has been measured at the
409 lower investigated σ'_v , while post-cyclic pullout resistance remains almost equal to the
410 corresponding static value at the higher σ'_v . To analyse the effects of cyclic loading on
411 the peak apparent coefficient of friction between soil and geosynthetic, $\mu_{s/GSY}^P$, generally
412 used in the design of reinforced earth structures, the comparison between $\mu_{s/GSY}^P$
413 evaluated under post-cyclic conditions ($A \approx 30\%$ P_R) and $\mu_{s/GSY}^P$ obtained by means of
414 CRD pullout tests is plotted in Figure 9b for soil-geogrid interface tested at different
415 vertical effective stresses. The experimental results show that the post-cyclic $\mu_{s/GSY}^P$
416 decreases with increasing σ'_v , as well as the apparent coefficient of friction under static
417 conditions, due to soil dilatancy at the interface. Moreover, σ'_v being equal, the apparent
418 coefficient of friction between soil and geosynthetic under post-cyclic conditions
419 decreases due to the effects of cyclic loading: the lower the vertical effective stress, the
420 higher the decrease (specifically, the reductions are equal to 28%, 16%, 5% and 2% for
421 $\sigma'_v = 10, 25, 50$ and 100 kPa respectively). This result is very important as pullout limit
422 state mainly affects the shallow reinforcement levels; therefore, if this decrease is not
423 taken into account, the earth works reinforced with geosynthetics could be wrongly
424 designed.

425 To better explain the reduction of the interface design parameters in post-cyclic
426 conditions, pullout loading P for varying pullout average strain ε for the i) CRD tests
427 carried out at all the investigated σ'_v (Figure 10a); ii) the MS tests performed at
428 $\sigma'_v = 100$ kPa, $A \approx 30$, 45% P_R and the corresponding CRD test (Figure 11a); and iii)
429 the MS tests performed at $\sigma'_v = 50$ kPa, $A \approx 30\%$ P_R and the corresponding CRD test
430 (Figure 12a) has been plotted. Before to comment these curves, it is necessary to start
431 by making a clarification: the application of cyclic tensile loading histories on geogrids
432 tested in-air do not induce a material degradation resulting in the reduction of the
433 geosynthetic's tensile strength, according to previous researches (Cardile et al., 2017b;
434 Kongkitkul et al., 2004; Vieira and Lopes, 2013). The main goal of the present research
435 is to comprehend whether or not the behaviour under cyclic pullout conditions (hence in
436 confined conditions) involves a degradation for the soil-geogrid interface resulting in
437 the reduction of the interface parameters (therefore, a reduction of the pullout
438 resistance). For this purpose, the $P - \varepsilon$ curves (Figure 10a, Figure 11a, Figure 12a) have
439 been plotted to represent the reinforcement's behaviour under soil confinement
440 condition (for fixed specimen length, test rate and temperature). The soil-geogrid
441 interaction provides $P - \varepsilon$ curves that are different for varying the pullout loading
442 conditions (monotonic or cyclic) and the vertical effective stress due to both soil
443 dilatancy at the interface and the reinforcement extensibility (i.e., stiffness). $P - \varepsilon$ curves
444 can relate to $\delta - \varepsilon$ curves (Figure 10b, Figure 11b, Figure 12b) in order to link the
445 displacement of the specimen's first confined section δ to the corresponding pullout
446 average strain value caused by a certain pullout load, for a fixed vertical effective stress.
447 With regard to CRD pullout tests (Figure 10b), when the soil-geogrid interface is in the
448 load transfer phase the $\delta - \varepsilon$ curve exhibits a pseudo-linear trend ($\sigma'_v = 100$ kPa), which

449 tends to curve during the pullout phase ($\sigma'_v = 10, 25, 50$ kPa) until reaching a vertical
450 asymptote for pullout failure (constant average strain with increasing δ). δ - ε slope
451 clearly depends only on test rate when the soil-geogrid interface is in the load transfer
452 phase. Once the pullout phase starts, δ - ε slope depends even on σ'_v since the pullout
453 resistances decrease with decreasing σ'_v (Figure 10a).

454 In pullout multi-stage tests, the first outcome arising from the observation of point 5
455 versus point 1 in Figure 11b and Figure 12b is that the cyclic loading application caused
456 both a higher geogrid's deformation (due to the geogrid's viscous effects resulting from
457 the application of a loading that can be considered constant on average over time) and a
458 higher head's displacement, with the MS δ - ε slope of the cyclic stage increasing with
459 increasing loading amplitude (pointed out in Figure 11b by means of an arrow-shaped
460 object). This means that the displacements of geogrid's internal points (along the length
461 of the specimen) at the beginning of the MS third phase (point 5) are higher than those
462 mobilised at the same pullout load level P_i (point 1) in the corresponding static test. For
463 a better knowledge, a qualitative trend is plotted in Figure 11c and Figure 12c (square c-
464 1): by comparing them, the lower the vertical effective stress, the higher the
465 displacements. These representations allow understanding how these higher
466 displacements obtained under cyclic loading move the interface towards a configuration
467 closer to pullout failure than the corresponding static test.

468 By analysing the third stage, Figure 11b and Figure 12b show that the MS δ - ε curve at
469 the beginning of this phase restarts with a trend similar to the one of CRD δ - ε curve at
470 the same strain level $\varepsilon_{0-2} = \varepsilon_{0-5}$ (point 5 versus point 2): trends get back similar as both
471 are now displacement-controlled pullout tests at the same test rate. Specifically, it looks
472 like the CRD δ - ε curve shifts down (path 5-7) of an amount δ_{2-5} equal to the difference

473 between the cyclic (δ_{1-5}) and the static (δ_{1-2}) displacements of the specimen's first
474 confined section reached at the same pullout average strain level (Figure 12b).
475 Moreover, during the third stage the interface tries again to mobilise the same pullout
476 strength that it would have mobilised if the cyclic stage hadn't occurred (reinforcement
477 has no degradation per se), showing a hardening curve (incremental pullout stiffness in
478 the path 5-6b is higher than the one in path 2-4, Figure 11a and Figure 12a). However,
479 this could be not possible since the cyclic loading contributed to use up more quickly
480 the geogrid's portion on which the mobilisation of the interaction mechanisms
481 withstands the applied load; that is, these cyclic loading effects (pointed out in Figure
482 11b and Figure 12b by means of an arrow-shaped object) could lead the interface a little
483 bit closer to the pullout failure, compared to an entirely monotonic loading. In fact, if
484 the development of the interaction mechanisms along the geogrid hadn't gone further,
485 the MS δ - ε curve would have followed the "ideal" trend (dash-dot line in path 5-7,
486 Figure 12b), i.e. the difference between MS and CRD displacements of the specimen's
487 first confined section reached at the same pullout average strain level would have
488 continued to be always δ_{2-5} (caused by the cyclic load application). Instead, the actual
489 MS δ - ε curve deviates from the "ideal" path 5-7 due to the cyclic loading effects,
490 which cause the interface degradation; this means that the geogrid starts to deform
491 fewer when a certain head's displacement is reached, mobilising a lower pullout
492 strength.

493 These cyclic loading effects can be appreciate better by considering the displacements
494 qualitative distribution of the geogrid's internal points when $\delta = 100$ mm has been
495 reached: Figure 11c and Figure 12c, square c-2 show that the displacements of the
496 geogrid's internal points representing 6b are higher than those representing 6a, and this

497 result is because the cyclic loading pushed towards the pullout process; in other words,
498 the geogrid starts to deform fewer approaching the pullout limit state earlier. Clearly,
499 the smaller the displacements of the geogrid's internal points, the more ideal the $\delta - \varepsilon$
500 trend.

501 Summarising, to reach the pullout average strain corresponding to the peak pullout
502 resistance P_R obtained under static conditions is theoretically always possible, unless
503 pullout failure occurs first (vertical asymptote). This assertion can be explained by
504 considering a fictitious extension of the MS $\delta - \varepsilon$ curve (dashed lines, Figure 11b and
505 Figure 12b): the soil-geogrid interface has to make a further head's displacement in
506 order to achieve P_R (i.e. the interface can mobilise P_R with a head's displacement
507 greater than the one under static condition). For instance, the interface tested at
508 $\sigma'_v = 100$ kPa would mobilise P_R with both the investigated amplitudes in case it could
509 carry out the further increment plotted in Figure 11b (δ_{6b-8} for $A \approx 30\% P_R$ and $\delta_{6'b-8'}$ for
510 $A \approx 45\% P_R$ respectively). This result affects the peak apparent coefficient of friction
511 between soil and geosynthetic; in fact, $\mu_{s/GSY}^P$ (Figure 9b) evaluated under post-cyclic
512 conditions ($A \approx 30\% P_R$) is almost equal to the one obtained in the corresponding static
513 pullout test for $\sigma'_v = 100$ kPa (only a very slight degradation of the interface occurred).
514 In case the limitation due to the clamp maximum displacement allowed by the
515 laboratory apparatus does not exist, the soil-geogrid interface analysed in this research
516 can mobilise P_R at $\sigma'_v = 100$ kPa even under post-cyclic loading with amplitudes up to
517 $A \approx 45\% P_R$.

518 Instead, for the interface at $\sigma'_v = 50$ kPa to reach the pullout average strain
519 corresponding to P_R is more difficult as the head's displacement to be done is much
520 higher (this increasing with decreasing vertical effective stress): the MS $\delta - \varepsilon$ trend is

521 curved (as well as the CRD one) as the pullout phase has been reached (Figure 12b) and
522 the displacements of the geogrid's internal points (6b trend in Figure 12c, square c-2)
523 are pushing further towards the achievement of pullout failure (that is, the cyclic loading
524 degraded the interface). This means that the pullout loading cannot increase further and,
525 consequently, $\mu_{s/GSY}^P$ evaluated under post-cyclic conditions is lower than $\mu_{s/GSY}^P$
526 obtained in the corresponding CRD pullout test.

527

528 **3.4 Nodal displacements**

529 Finally, in order to explain the different behaviour of the soil-reinforcement interface
530 when the cyclic loading generates a load transfer mechanism or the pullout failure, the
531 actual distributions of the transversal rib displacements along the geogrid for different
532 numbers of cycles have been plotted in Figure 13a,b, for $A \approx 30\% P_R$ and
533 $\sigma'_v = 10$ and 100 kPa respectively. In Figure 13a, for vertical effective stress equal to
534 10 kPa, it is possible to observe that the reinforcement almost reached the pullout limit
535 state during the cyclic stage (two adjacent curves are parallel to each other), with the
536 third stage still being allowed (as the reached head's displacement is lower than 100
537 mm). This means that the cyclic loading entailed a significant reduction of the pullout
538 resistance during the CRD third stage, caused by higher displacements along the
539 geogrid that pushed towards the pullout failure. Since the mobilised soil shear-strength
540 angle depends on soil-geogrid relative sliding, the interaction mechanisms along the
541 interface's points (Bergado et al., 1993; Calvarano et al., 2014; Cardile et al., 2017a;
542 Dyer, 1985; Jacobs et al., 2014; Moraci et al., 2017; Palmeira, 2009; Sieira et al., 2009;
543 Zhou et al., 2012; Ziegler and Timmers, 2004) mobilised pullout strengths lower than
544 those mobilised under static conditions. These values are as close as possible to the

545 lowest that can be reached under static conditions, i.e. they are characteristic of the
546 residual phase in the pullout static curve at $\sigma'_v = 10$ kPa (strain-softening pullout
547 behaviour at lower σ'_v as shown in Moraci and Recalcati, 2006). On the other hand, for
548 $\sigma'_v = 100$ kPa, the reinforcement is still in the load transfer phase when the cyclic stage
549 is over: the interaction mechanisms developed a pullout mechanism along the active
550 length that is markedly progressive (Figure 13b). In this case, a “supply” of resistance is
551 still available in the post-cyclic stage for all the above reasons. The interaction
552 mechanisms mobilised strength values almost equal to P_R , which happens to coincide
553 with the ultimate resistance that can be reached, as the CRD curve at $\sigma'_v = 100$ kPa
554 exhibits a strain-hardening pullout behaviour (typical of higher vertical effective
555 stresses as shown in Moraci and Recalcati, 2006).

556 **4 CONCLUSIONS**

557 The paper deals with the results of several pullout tests carried out on an HDPE
558 geogrid-granular soil interface subjected to multi-stage loading conditions and different
559 vertical effective stresses ($\sigma'_v = 10, 25, 50, 100$ kPa). Cyclic and post-cyclic conditions
560 were investigated by means of a multistage procedure, applying different cyclic loading
561 histories characterised by a high frequency ($f=1$ Hz).

562 To define when the behaviour of soil-reinforcement interface is stable/unstable from a
563 point of view linked to the cyclic loadings application, a criterion has been established.

564 The results have showed that the soil-geogrid interface behaviour is dependent on both
565 the cyclic loading amplitude and vertical effective stress. The stability of soil-geogrid
566 interface during the cyclic phase starts getting worse with increasing cyclic loading

567 amplitude, entailing the possible achievement of the pullout limit state, while the
568 increasing of the vertical effective stress σ'_v plays a stabilising role.

569 The analysis of the cumulative strain mobilised in the specimen at the end of each
570 corresponding cycle highlighted that it increases with increasing cyclic loading
571 amplitude and numbers of cycles and, N being equal, increases with increasing vertical
572 effective stress. By comparing the results of residual strain evaluated for the geogrid's
573 monitored portion closer to its head with those obtained by wide-width tensile multi-
574 stage tests, the pullout cyclic residual strain happens to be higher since the average test
575 rate of pullout MS tests is lower due to the soil confinement.

576 With regard to pullout resistances, the results have showed that cyclic loading histories
577 can involve a reduction of the interface parameters considering a certain combination of
578 vertical effective stress and cyclic loading amplitude A , for the investigated frequency:
579 the lower the vertical effective stress, the higher the reduction, A being equal. For the
580 specific test conditions, the post-cyclic peak pullout resistance reaches decreases up to
581 28% at the lower σ'_v investigated, while it remains almost equal to the corresponding
582 monotonic value at the higher σ'_v .

583 The decreasing of the interface parameters can be explained by the progressive pullout
584 mechanism of the soil-geogrid interface: the load is transferred on a geogrid's portion
585 that increases quickly during the cyclic phase, involving a reduction of the "supply" of
586 pullout resistance during the post-cyclic phase that increases with decreasing vertical
587 effective stress and with increasing cyclic loading amplitude. To reach the static peak
588 pullout resistance P_R is theoretically always possible even under cyclic conditions,
589 unless pullout failure occurs: the interface can mobilise P_R with a head's displacement
590 greater than the one under static condition.

591 The preferred option to design GRS structures in the best way possible would be to use
592 peak apparent coefficients of friction between soil and geosynthetic, $\mu_{s/GSY}^P$, varying
593 with the depth where the reinforcement is embedded. If it be so, since pullout limit state
594 mainly affects the shallow reinforcement levels, the $\mu_{s/GSY}^P$ reduction arising under
595 possible cyclic loading has to be taken into account. Specifically, the lower the vertical
596 effective stress, the higher the reduction.

597

598

List of notation

A	Cyclic tensile loading amplitude (kN/m)
CRD	Constant rate of displacement (mm/min)
CSR	Constant strain rate (%/min)
D_{50}	Average grain size (mm)
f	Frequency of cyclic load (Hz)
GRS	Geosynthetic-reinforced soil (-)
$HDPE$	High-density polyethylene (-)
$J_{sec\ 2\%}$	Secant tensile stiffness at 2% strain (0.2%/min strain rate) (kN/m)
$J_{sec\ 2\% (ISO)}$	Secant tensile stiffness at 2% strain (20%/min strain rate, STANDARD ISO 10319) (kN/m)
L_R	Length of geogrid (m)
MS	Multi-stage (-)
N	Number of cycles (-)
P	Pullout load per unit width (kN/m)
P_i	Pullout load (per unit width) representative of serviceability conditions (kN/m)
P_R	Peak pullout resistance (per unit width) obtained by pullout tests under static conditions (kN/m)
P_R^{PC}	Peak pullout resistance (per unit width) obtained by pullout tests under multi-stage conditions (kN/m)
RH	Relative humidity (%)
T_{max}	Maximum tensile strength per unit width (monotonic test at 0.2%/min strain rate) (kN/m)
$T_{max (ISO)}$	Maximum tensile strength per unit width (monotonic test at 20%/min strain rate, STANDARD ISO 10319) (kN/m)
U	Uniformity coefficient (-)
w_{opt}	Optimum water content (%)
γ_d	Dry unit weight (kN/m ³)
$\gamma_{d\ max}$	Maximum dry unit weight (kN/m ³)
δ	Displacement of the first confined section of specimen (mm)
$\Delta\delta_i^e$	Cumulative cyclic displacement of the specimen's rear end (mm)
$\Delta\delta_i^h$	Cumulative cyclic displacement of the specimen's first confined section (mm)
$\Delta\delta_{part,i}^e$	Cyclic displacement's increment of the specimen's rear end reached during each cyclic loading (mm)
$\Delta\delta_{part,i}^h$	Cyclic displacement's increment of the specimen's head reached during each cyclic loading (mm)

ε	Pullout average strain (%)
ε_{\max}	Tensile strain for T_{\max} (monotonic test at 0.2%/min strain rate) (%)
$\varepsilon_{\max}(\text{ISO})$	Tensile strain for $T_{\max}(\text{ISO})$ (monotonic test at 20%/min strain rate, STANDARD ISO 10319) (%)
ε_r	Residual strains caused by cyclic loading when the cyclic loading returns to Pi (%)
ε'	Strain rate (%/min)
$\mu_{S/GSY}^P$	Peak apparent coefficients of friction between soil and geosynthetic (-)
σ_v'	Vertical effective stress (kN/m ²)
ϕ_p'	Soil peak shear-strength angle (°)
ϕ_{cv}'	Soil shear-strength angle at constant volume (°)

600 **Tables**

601 *Table 1 Wide-width tensile test results of the geogrid used in this research.*

$T_{\max (ISO)}$	T_{\max}	$\mathcal{E}_{\max (ISO)}$	\mathcal{E}_{\max}	$J_{\text{sec } 2 \% (ISO)}$	$J_{\text{sec } 2 \%}$
[kN/m]	[kN/m]	[kN/m]	[kN/m]	[kN/m]	[kN/m]
($\varepsilon' = 20 \%$ per minute)	($\varepsilon' = 0.2 \%$ per minute)	($\varepsilon' = 20 \%$ per minute)	($\varepsilon' = 0.2 \%$ per minute)	($\varepsilon' = 20 \%$ per minute)	($\varepsilon' = 0.2 \%$ per minute)
159	103.5	12.2	14.5	2454	1525

602

603

604

605 *Table 2 MS pullout testing plan.*

Test	N (planned)	N (actually- made)	σ'_v [kPa]	P_i [kN/m]	A [kN/m]
01	1000	1000	10	$\approx 35\%P_R$ (10 kPa)	$\approx 30\%P_R$ (10 kPa)
02	1000	20	10	$\approx 35\%P_R$ (10 kPa)	$\approx 45\%P_R$ (10 kPa)
03	1000	1000	25	$\approx 35\%P_R$ (25 kPa)	$\approx 30\%P_R$ (25 kPa)
04	1000	148	25	$\approx 35\%P_R$ (25 kPa)	$\approx 45\%P_R$ (25 kPa)
05	1000	1000	50	$\approx 35\%P_R$ (50 kPa)	$\approx 30\%P_R$ (50 kPa)
06	1000	158	50	$\approx 35\%P_R$ (50 kPa)	$\approx 45\%P_R$ (50 kPa)
07	1000	1000	100	$\approx 35\%P_R$ (100 kPa)	$\approx 30\%P_R$ (100 kPa)
08	1000	1000	100	$\approx 35\%P_R$ (100 kPa)	$\approx 45\%P_R$ (100 kPa)

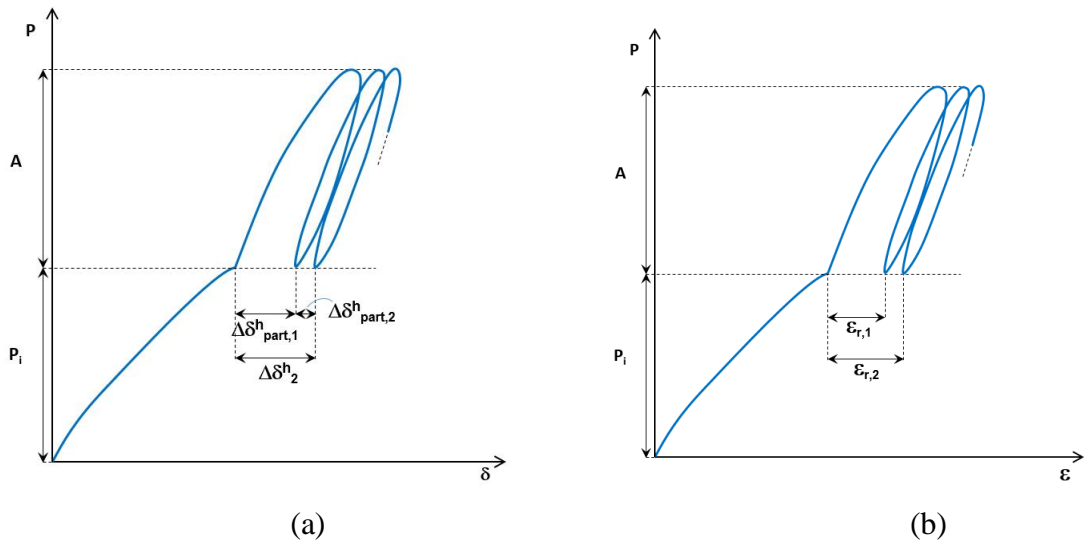
606

607



611 *Figure 1. Apparatus used for pullout testing: pullout steel box (a); soil-geogrid*
612 *specimen and LVDT (b); air bag (c); clamp and sleeves (d), hydraulic actuator and*
613 *load cell (e).*

615

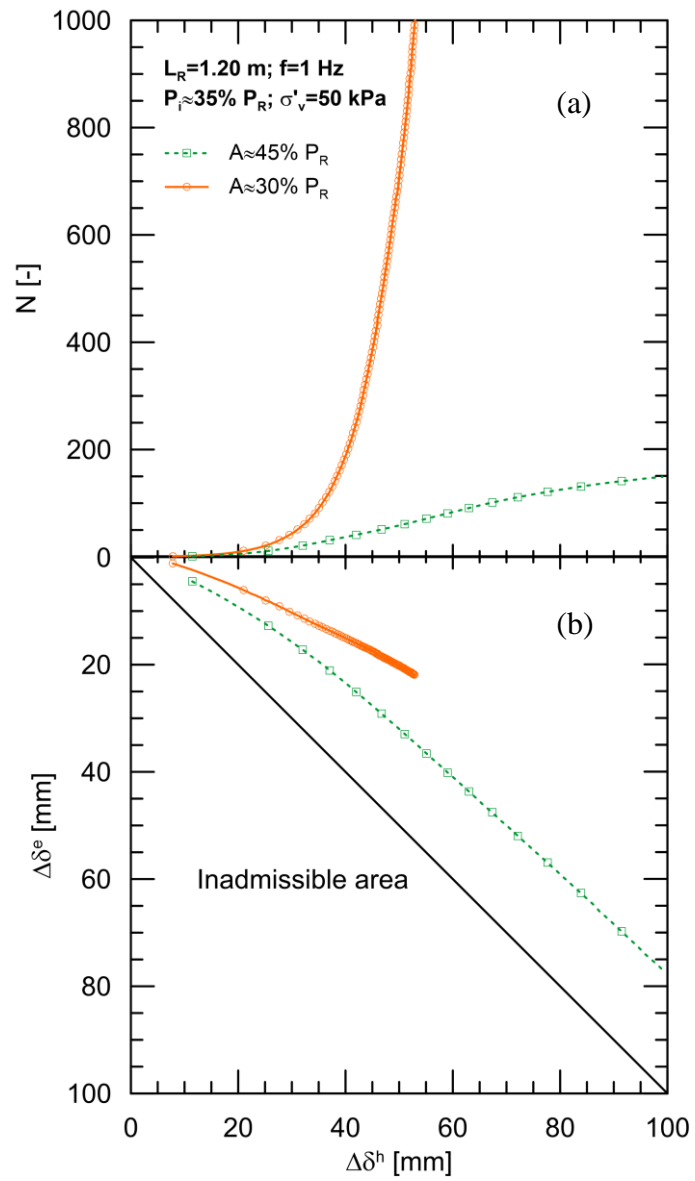


616

617 *Figure 2. Schematic representation of different parameters obtained during hysteresis*

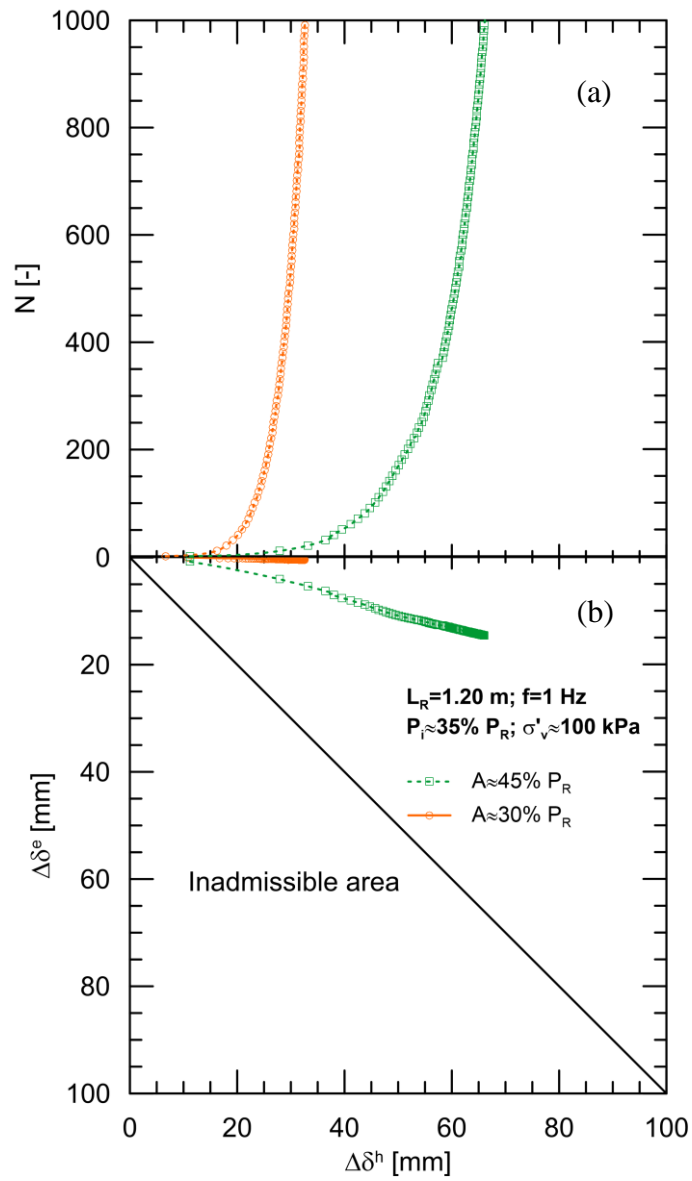
618 *loops in multi-stage tests: P-δ plane (a); P-ε plane (b).*

619



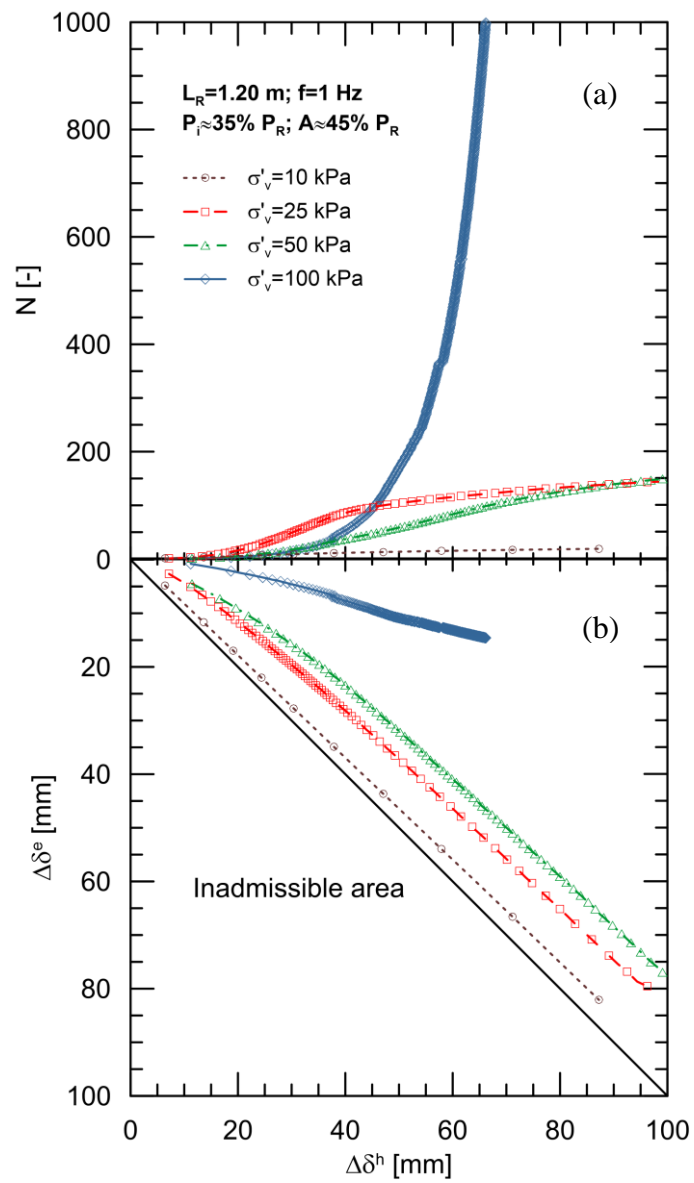
621

622 *Figure 3. Number of loading cycles versus cumulative cyclic displacement measured at*623 *the first confined section of specimen (a), and $\Delta\delta^h$ versus cumulative cyclic*624 *displacement measured at the rear end of the specimen (b) for $A \approx 30\% P_R$, $45\% P_R$ and*625 *$\sigma'_v = 50$ kPa.*



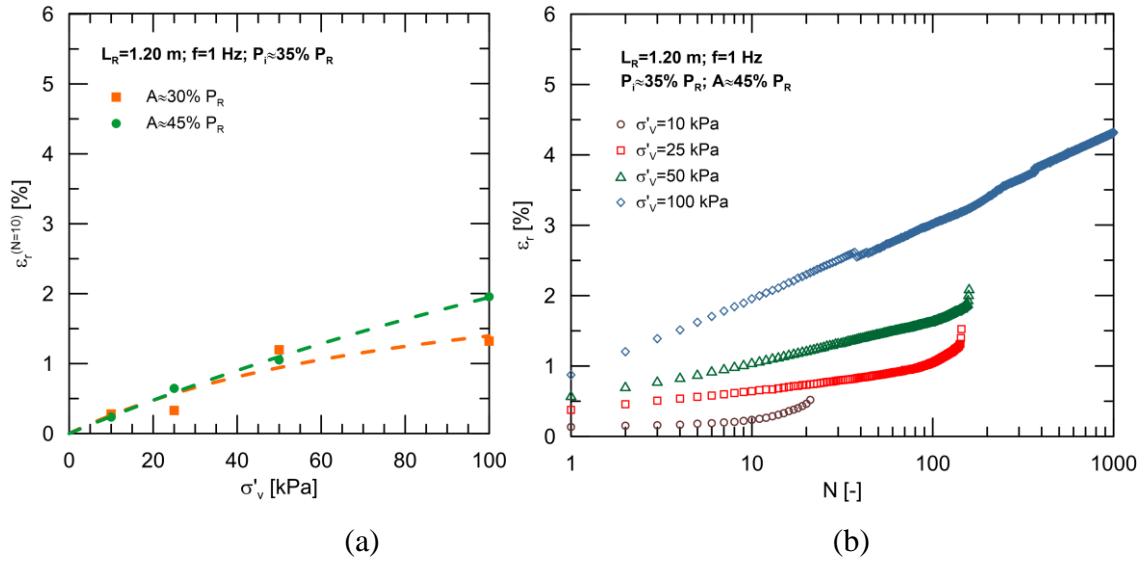
627

628 *Figure 4. Number of loading cycles versus cumulative cyclic displacement measured at*629 *the first confined section of specimen (a), and $\Delta\delta^h$ versus cumulative cyclic*630 *displacement measured at the rear end of the specimen (b) for $A \approx 30\% P_R$, $45\% P_R$ and*631 *$\sigma'_v = 100$ kPa.*



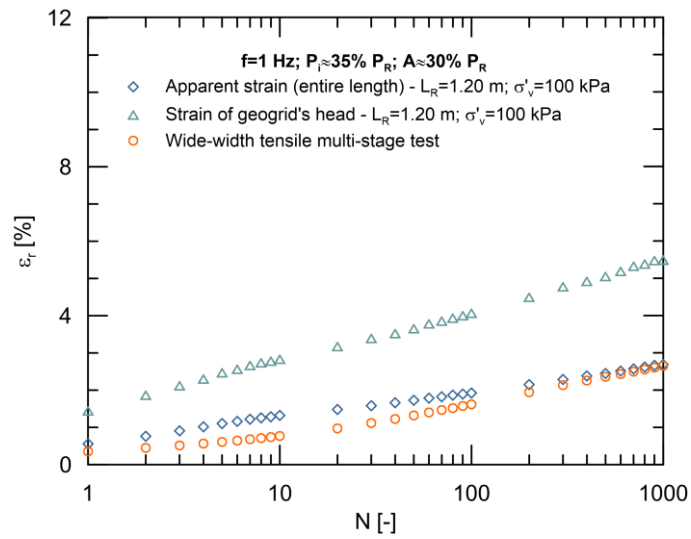
633

634 *Figure 5. Number of loading cycles versus cumulative cyclic displacement of the*
 635 *specimen's first confined section (a) and $\Delta\delta^e$ versus cumulative cyclic displacement of*
 636 *the specimen's rear end (b) for varying σ'_v at $A \approx 45\% P_R$.*

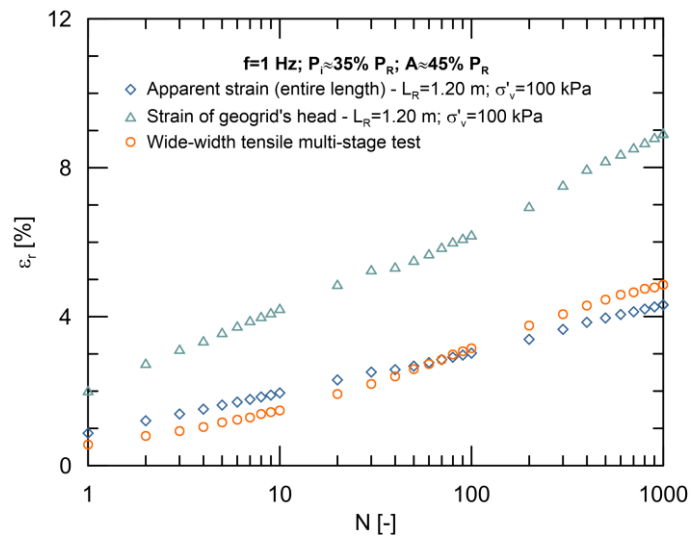


638

639 *Figure 6. Residual strain at loading cycle $N = 10$ versus vertical effective stress, for*
 640 *$A \approx 30\% P_R$ and $45\% P_R$ (a); and residual strain for varying number of loading cycles*
 641 *at different vertical effective stresses and $A \approx 45\% P_R$ (b).*



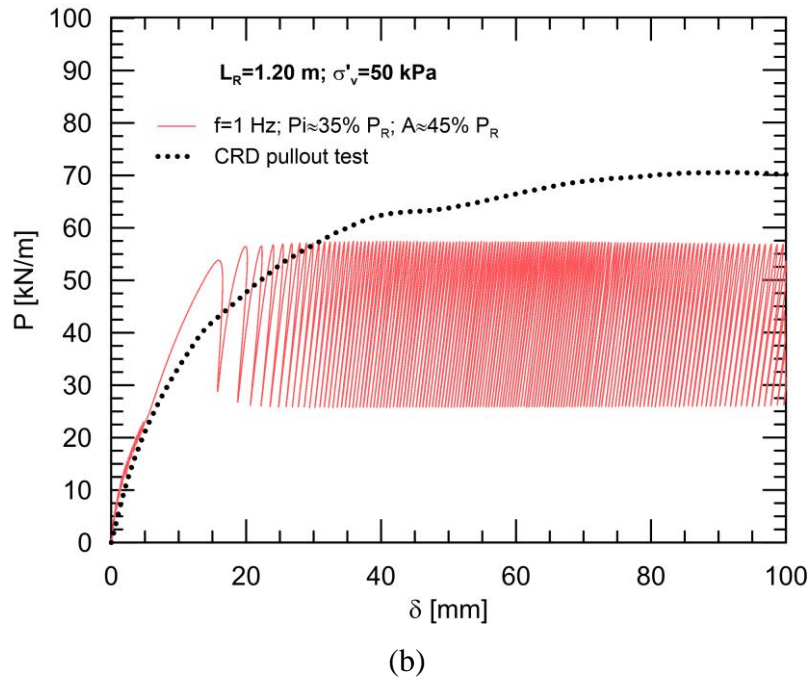
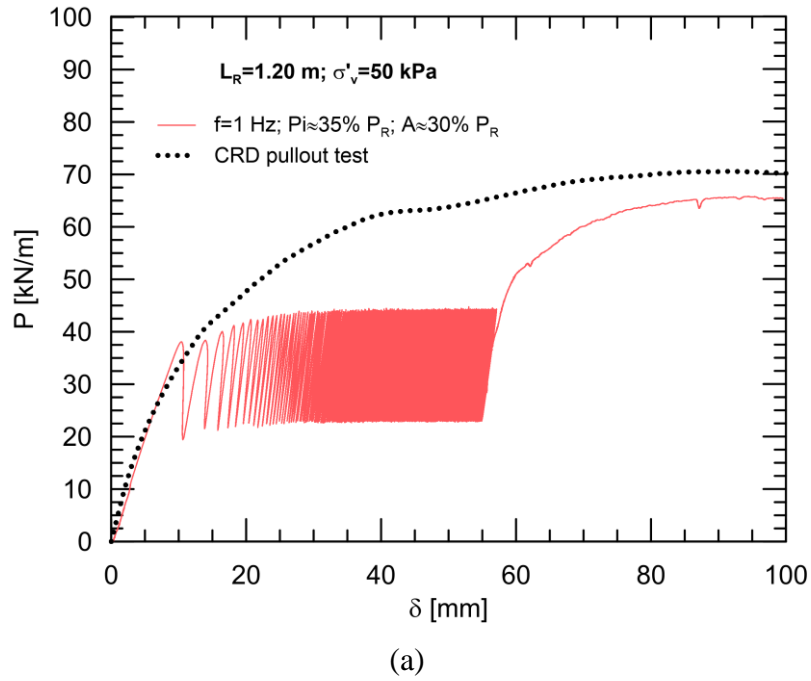
(a)



(b)

643

644 *Figure 7. Residual strain evaluated for the entire length of the geogrid and its*645 *monitored portion closer to the head, for varying number of loading cycles at*646 *$\sigma'_v = 100$ kPa, $A \approx 30\% P_R$ (a) and $\sigma'_v = 100$ kPa, $A \approx 45\% P_R$ (b), and comparison with*647 *the corresponding wide-width tensile tests.*

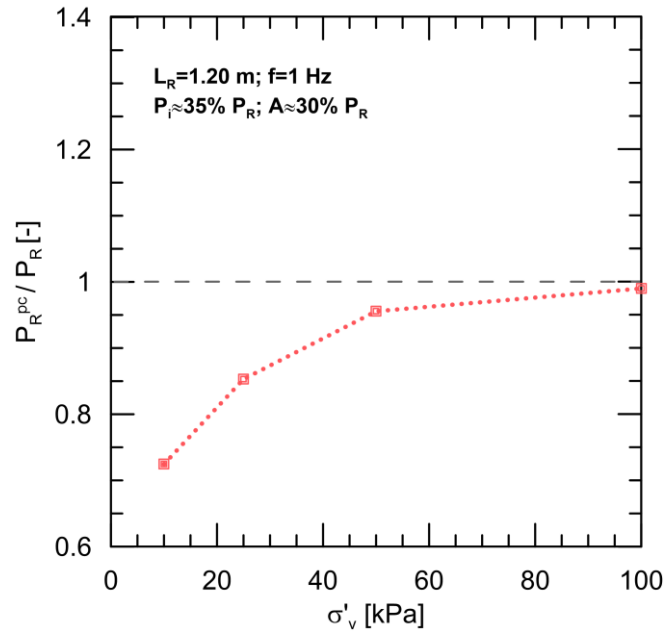


649

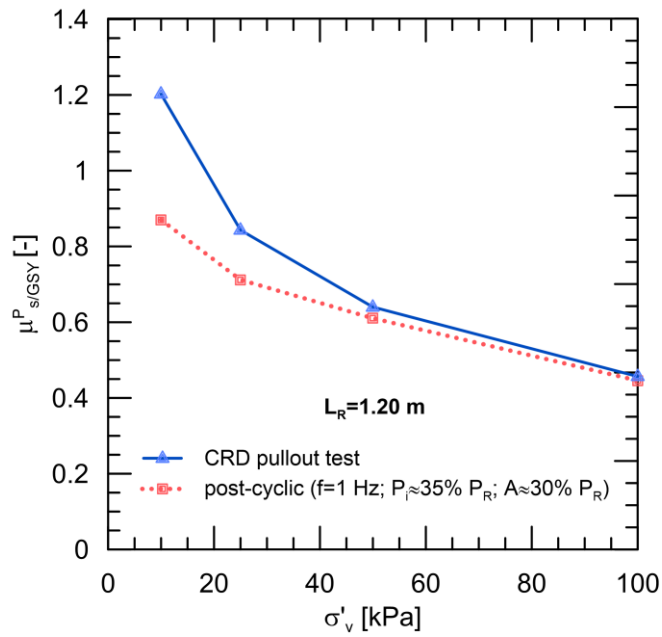
650 *Figure 8. Comparison between load-displacement trends obtained in CRD and*

651 *multistage conditions for tests with $\sigma'_v = 50$ kPa, at $A \approx 30\% P_R$ (a) and $A \approx 45\% P_R$ (b)*

652 *respectively.*

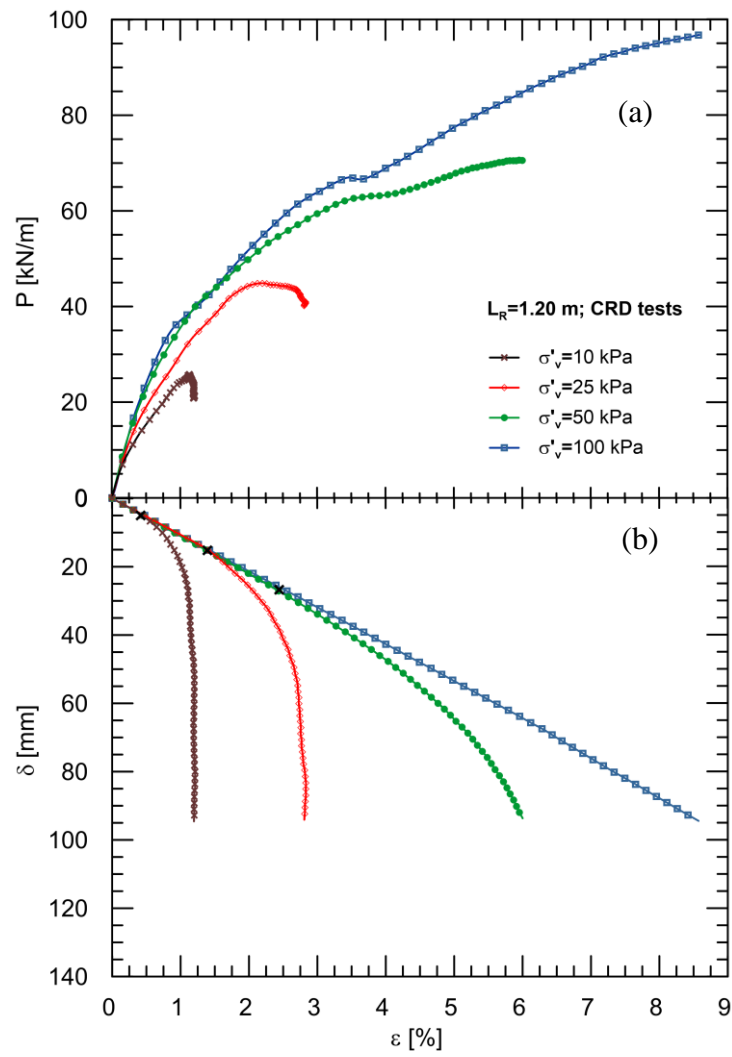


(a)

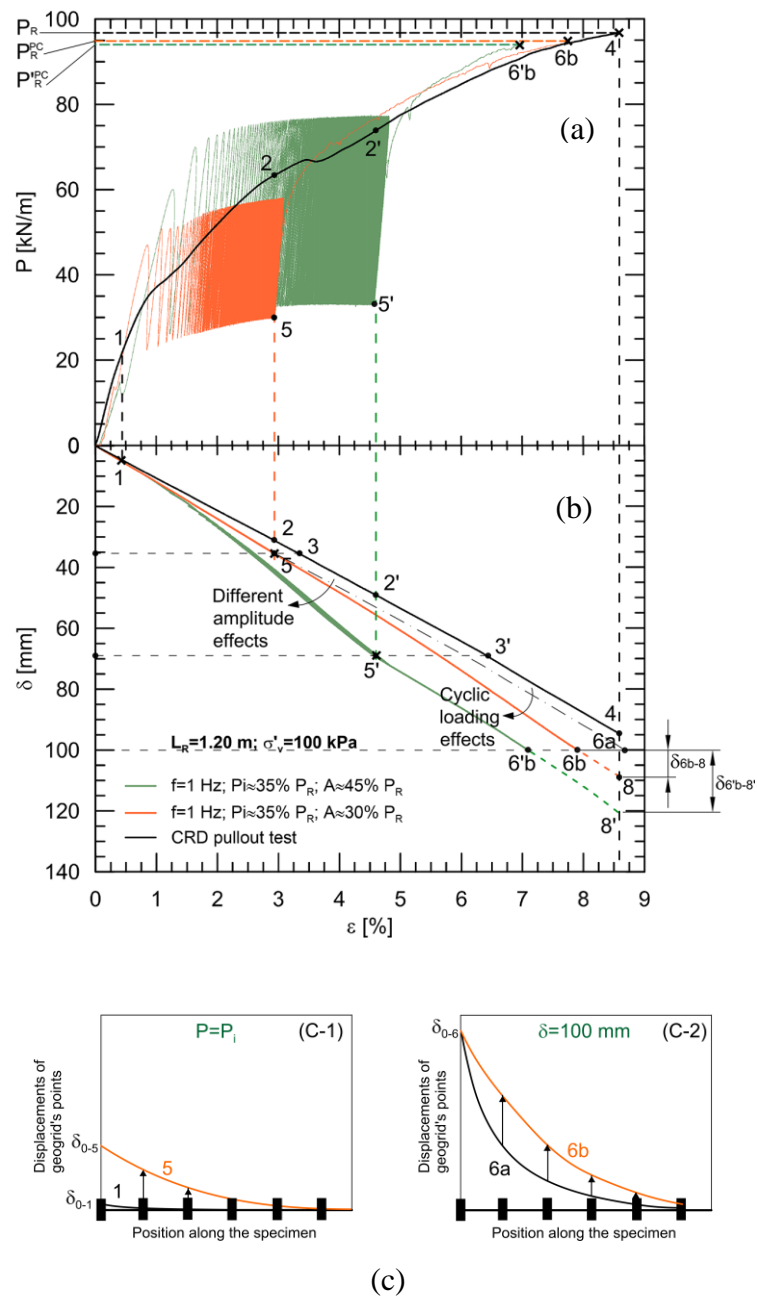


(b)

655 *Figure 9. Normalised post-cyclic peak pullout resistance (a) and peak apparent*
 656 *coefficient of friction (b) for varying vertical effective stress, considering CRD and*
 657 *multi-stage tests at $A \approx 30\% P_R$.*



660 *Figure 10. P- ϵ (a) and δ - ϵ (b) trends obtained in CRD conditions for different vertical*
 661 *effective stresses.*



662

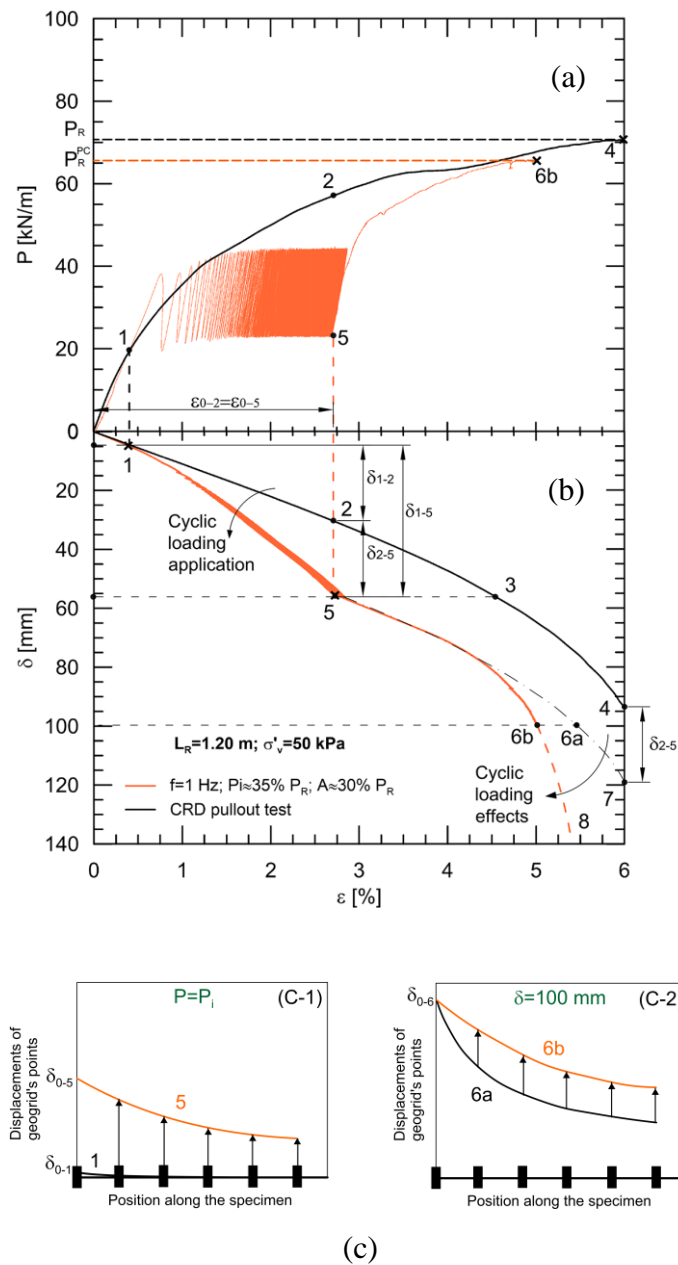
663 *Figure 11. Comparison between P - ε (a) and δ - ε (b) trends obtained in CRD and*

664 *multistage conditions for tests with $\sigma'_v = 100$ kPa, at $A \approx 30$ - 45% P_R , and qualitative*

665 *distribution of the geogrid's points displacements at the same pullout load level P_i for*

666 *CRD test and MS test at $N=1000$ (c-1) and at $\delta = 100$ mm for MS test following the*

667 *"ideal" or the real path (c-2).*



668

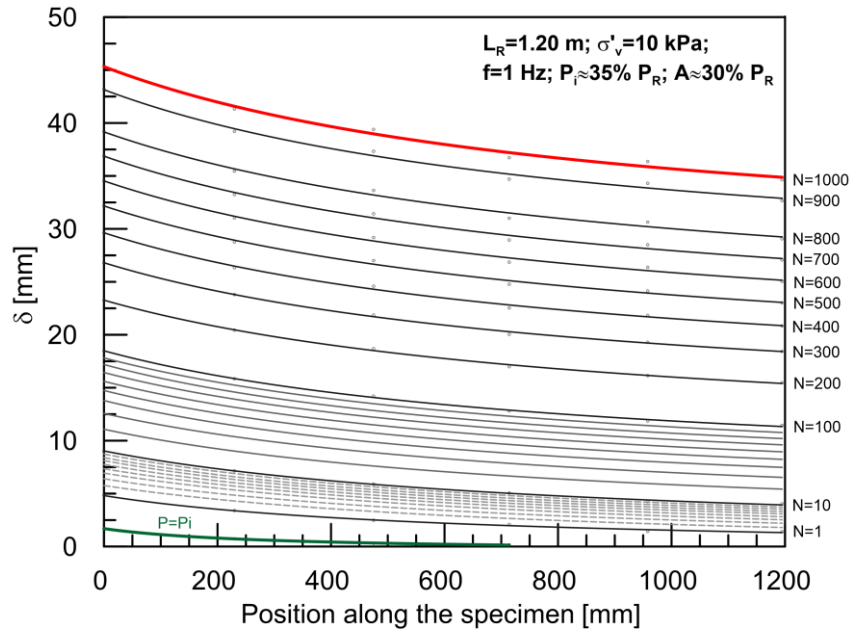
669 *Figure 12. Comparison between P - ϵ (a) and δ - ϵ (b) trends obtained in CRD and*

670 *multistage conditions for tests with $\sigma'_v = 50$ kPa, at $A \approx 30\% P_R$, and qualitative*

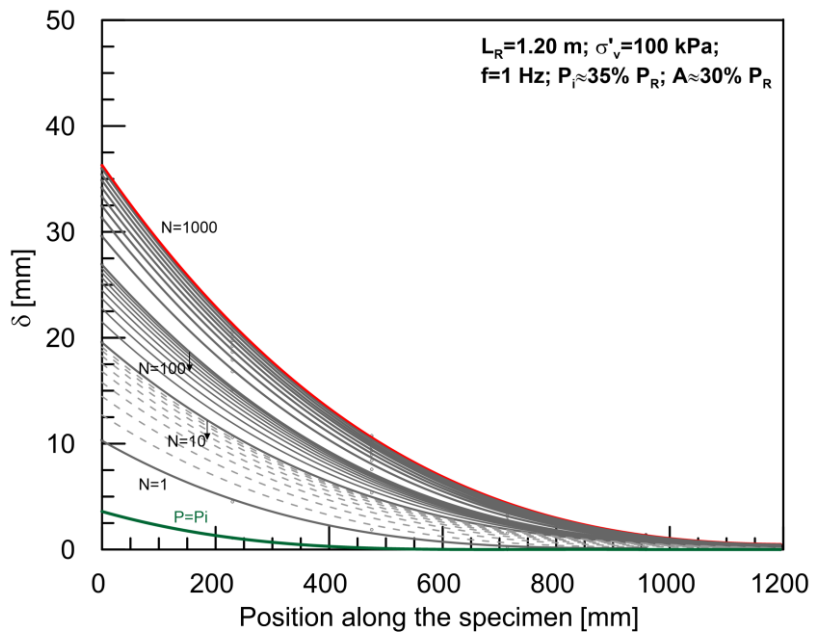
671 *distribution of the geogrid's points displacements at the same pullout load level P_i for*

672 *CRD test and MS test at $N=1000$ (c-1) and at $\delta = 100$ mm for MS test following the*

673 *"ideal" or the real path (c-2).*



(a)



(b)

675

676 *Figure 13. Distributions of the nodal displacements along the reinforcement for*
 677 *different numbers of cycles, for specimens tested at $A \approx 30\% P_R$ and $\sigma'_v = 10 \text{ kPa}$ (a);*
 678 *$A \approx 30\% P_R$ and $\sigma'_v = 100 \text{ kPa}$ (b) respectively.*

680

681 **5 REFERENCES**

682 AASHTO T 99, 2015. Standard Method of Test for Moisture-Density Relations of Soils
683 Using a 2.5-kg (5.5-lb) Rammer and a 305-mm (12-in.) Drop, American Association of
684 State Highway and Transportation Officials (AASHTO), Washington, DC, USA.

685 ASTM D2487-17, 2017. Standard Practice for Classification of Soils for Engineering
686 Purposes (Unified Soil Classification System), ASTM International, West
687 Conshohocken, PA.

688 Abramento, M., 1995. Analysis of pullout tests for planar reinforcements in soil. Journal
689 of Geotechnical Engineering 121 (6), 476-485.

690 Alonso-Marroquín, F., Herrmann, H.J., 2004. Ratcheting of Granular Materials.
691 Physical Review Letters 92 (5), 543011-543014.

692 ASTM D1557-12e1, 2012. Standard Test Methods for Laboratory Compaction
693 Characteristics of Soil Using Modified Effort (56,000 ft-lbf/ft³ (2,700 kN-m/m³)),
694 ASTM, West Conshohocken, PA, USA

695 ASTM D698-12e2, 2012. Standard Test Methods for Laboratory Compaction
696 Characteristics of Soil Using Standard Effort (12 400 ft-lbf/ft³ (600 kN-m/m³)), ASTM,
697 West Conshohocken, PA, USA

698 Ausilio, E., Conte, E., Dente, G., 2000. Seismic stability analysis of reinforced slopes.
699 Soil dynamics and earthquake engineering 19, 159-172.

700 Bathurst, R.J., Allen, T., Walters, D., 2004. Reinforcement loads in geosynthetic walls
701 and the case for a new working stress design method, Mercer Lecture. 3rd European
702 Geosynthetics Conference Eurogeo 3, Monaco, Germany, pp. 19-32.

703 Bathurst, R.J., Cai, Z., 1995. Pseudo-static seismic analysis of geosynthetic-reinforced
704 segmental retaining walls. *Geosynthetics International* 2 (5), 787-830.

705 Bathurst, R.J., Ezzein, F.M., 2017. Insights into geogrid–soil interaction using a
706 transparent granular soil. *Géotechnique Letters* 7, 179-183.

707 Bergado, D.T., Shivashankar, R., Alfaro, M.C., Chai, J.-C., Balasubramaniam, A.S.,
708 1993. Interaction behaviour of steel grid reinforcements in a clayey sand. *Geotechnique*
709 43 (4), 589-603.

710 Biondi, G., Cascone, E., Maugeri, M., 2014. Displacement versus pseudo-static
711 evaluation of the seismic performance of sliding retaining walls. *Bulletin of Earthquake*
712 *Engineering*, 12(3), 1239-1267.

713 Cai, Z., Bathurst, R.J., 1996a. Deterministic sliding block methods for estimating
714 seismic displacements of earth structures. *Soils Dynamics and Earthquake Engineering*
715 15, 255-268.

716 Cai, Z., Bathurst, R.J., 1996b. Seismic-induced permanent displacement of
717 geosynthetic-reinforced segmental retaining walls. *Canadian Geotechnical Journal* 33,
718 937-955.

719 Calvarano, L.S., Giofrè, D., Cardile, G., Moraci, N., 2014. A stress transfer model to
720 predict the pullout resistance of extruded geogrids embedded in compacted granular
721 soils, 10th International Conference on Geosynthetics, ICG 2014, Berlin, Germany.

722 Calvetti, F., di Prisco, C., 2010. Discrete numerical investigation of the ratcheting
723 phenomenon in granular materials. *Comptes Rendus Mécanique* 338 (10-11), 604-614.

724 Capilleri, P.P., Ferraiolo, F., Motta, E., Scotto, M., Todaro, M., 2019. Static and
725 dynamic analysis of two mechanically stabilized earth walls. *Geosynthetics*
726 *International*.

727 Carbone, L., Gourc, J.P., Carrubba, P., Pavanello, P., Moraci, N., 2015. Dry friction
728 behaviour of a geosynthetic interface using inclined plane and shaking table tests.
729 *Geotextiles and Geomembranes* 43 (4), 293-306.

730 Cardile, G., Calvarano, L.S., Giofrè, D., Moraci, N., 2014. Experimental evaluation of
731 the pullout active length of different geogrids, 10th International Conference on
732 *Geosynthetics*, ICG 2014, Berlin, Germany.

733 Cardile, G., Giofrè, D., Moraci, N., Calvarano, L.S., 2017a. Modelling interference
734 between the geogrid bearing members under pullout loading conditions. *Geotextiles and*
735 *Geomembranes* 45 (3), 169-177.

736 Cardile, G., Moraci, N., Calvarano, L.S., 2016a. Geogrid pullout behaviour according to
737 the experimental evaluation of the active length. *Geosynthetics International* 23 (2),
738 194-205.

739 Cardile, G., Moraci, N., Pisano, M., 2016b. In-air Tensile Load-strain Behaviour of
740 HDPE Geogrids Under Cyclic Loading. *Procedia Engineering* 158, 266-271.

741 Cardile, G., Moraci, N., Pisano, M., 2017b. Tensile behaviour of an HDPE geogrid
742 under cyclic loading: experimental results and empirical modelling. *Geosynthetics*
743 *International* 24 (1), 95-112.

744 Carrubba, P., Colonna, P., 2000. A comparison of numerical methods for multi-tied
745 walls. *Computers and Geotechnics* 27 (2), 117-140.

746 Carrubba, P., Montanelli, F., Moraci, N., 2000. Long-term behaviour of an instrumented
747 wall reinforced with geogrids, 2nd European Conference on Geosynthetics, Bologna,
748 Italy.

749 Di Filippo G., Biondi G., Moraci N., 2019. Seismic performance of geosynthetic-
750 reinforced retaining walls: experimental tests VS numerical predictions. 7th
751 International Conference on Earthquake Geotechnical Engineering.

752 Dyer, M.R., 1985. Observations of the stress distribution in crushed glass with
753 applications to soil reinforcement, Magdalene College. University of Oxford,
754 Michaelmas Term, Ph.D. Thesis, p. 220.

755 El-Emam, M.M., Bathurst, R.J., 2004. Experimental design, instrumentation and
756 interpretation of reinforced soil wall response using a shaking table. International
757 Journal of Physical Modelling in Geotechnics 4, 13-32.

758 El-Emam, M.M., Bathurst, R.J., 2005. Facing contribution to seismic response of
759 reduced-scale reinforced soil walls. Geosynthetics International 12 (6), 344-344.

760 Franca, F.A.N., Bueno, B.S., 2011. Creep behavior of geosynthetics using confined
761 accelerated tests. Geosynthetics International 18 (5), 242-254.

762 Gaudio, D., Masini, L., Rampello, S., 2018. A performance-based approach to design
763 reinforced-earth retaining walls. Geotextiles and Geomembranes 46 (4), 470-485.

764 Hatami, K., Bathurst, R.J., 2000. Effect of structural design on fundamental frequency
765 of reinforced-soil retaining walls. Soil dynamics and earthquake engineering 19, 137-
766 157.

767 Hirakawa, D., Kongkitkul, W., Tatsuoka, F., Uchimura, T., 2003. Time-dependent
768 stress–strain behaviour due to viscous properties of geogrid reinforcement.
769 *Geosynthetics International* 10 (6), 176-199.

770 Huang, C.-C., Chou, L.H., Tatsuoka, F., 2003. Seismic displacements of geosynthetic-
771 reinforced soil modular block walls. *Geosynthetics International* 10 (1), 2-23.

772 ISO 10319:2015. Geosynthetics Wide-width Tensile Test. International Organization for
773 Standardization, Geneva, Switzerland.

774 Izawa, J., Kuwano, J., Ishihara, Y., 2004. Centrifuge tilting and shaking table tests on
775 the RSW with different soils, 3rd Asian Regional Conference on Geosynthetics, Seoul,
776 Korea, pp. 803-810.

777 Jacobs, F., Ziegler, M., Vollmert, L., Ehrenberg, H., 2014. Explicit design of geogrids
778 with a nonlinear interface model, X International conference on Geosynthetics, Berlin,
779 Germany.

780 Jewell, R.A., 1990. Reinforcement bond capacity. *Geotechnique* 40 (3), 513-518.

781 Kongkitkul, W., Hirakawa, D., Tatsuoka, F., Uchimura, T., 2004. Viscous deformation
782 of geosynthetic reinforcement under cyclic loading conditions and its model simulation.
783 *Geosynthetics International* 11, 73-99.

784 Kongkitkul, W., Tatsuoka, F., Hirakawa, D., 2007a. Effects of reinforcement type and
785 loading history on the deformation of reinforced sand in plane strain compression. *Soils
786 and foundations* 47 (2), 395-414.

787 Kongkitkul, W., Tatsuoka, F., Hirakawa, D., 2007b. Rate-dependent load-strain
788 behaviour of geogrid arranged in sand under plane strain compression. *Soils and
789 foundations* 47 (3), 473-491.

790 Koseki, J., Bathurst, R.J., Guler, E., Kuwano, J., Maugeri, M., 2006. Seismic stability of
791 reinforced soil walls, 8th International Conference on Geosynthetics, Yokohama. Japan.

792 Koseki, J., Nakajima, S., Tateyama, M., Watanabe, K., Shinoda, M., 2009. Seismic
793 performance of geosynthetic-reinforced soil retaining walls and their performance-base
794 design in Japan, Performance-Based Design in Earthquake Geotechnical Engineering,
795 Tokyo, Japan.

796 Lee, K.Z.Z., Chang, N.Y., Ko, H.Y., 2010. Numerical simulation of geosynthetic-
797 reinforced soil walls under seismic shaking *Geotextiles and Geomembranes* 28 (4), 317-
798 334.

799 Leshchinsky, D., 2009. On Global Equilibrium in Design of Geosynthetic Reinforced
800 Walls. *Journal of Geotechnical and Geoenvironmental Engineering* 135 (3), 309-315.

801 Leshchinsky, D., Ling, H., Hanks, G., 1995. Unified design approach to geosynthetics
802 reinforced slopes and segmental walls. *Geosynthetics International* 2 (5), 845-881.

803 Leshchinsky, D., Kang, B., Han, J., Ling, H., 2014. Framework for Limit State Design
804 of Geosynthetic-Reinforced Walls and Slopes. *Transportation Infrastructure*
805 *Geotechnology* 1, 129-164.

806 Ling, H., Leshchinsky, D., 2005. Failure Analysis of Modular-Block Reinforced-Soil
807 Walls during Earthquakes. *Journal of Performance of Constructed Facilities* 19 (2), 117-
808 123.

809 Ling, H.I., Leshchinsky, D., Chou, N.N.S., 2001. Post-earthquake investigation on
810 several geosynthetic-reinforced soil retaining walls and slopes during the Ji-Ji
811 earthquake of Taiwan. *Soil dynamics and earthquake engineering* 21, 297-313.

812 Ling, H.I., Leshchinsky, D., Perry, E.B., 1997. Seismic design and performance of
813 geosynthetic-reinforced soil structures. *Geotechnique* 47 (5), 933-952.

814 Ling, H.I., Liu, H., Kaliakin, V.N., Leshchinsky, D., 2004. Analyzing Dynamic
815 Behavior of Geosynthetic-Reinforced Soil Retaining Walls. *Journal of Engineering*
816 *Mechanics* 130 (8), 911-920.

817 Ling, H.I., Mohri, Y., Kawabata, T., 1998. Tensile Properties of Geogrids Under Cyclic
818 Loadings. *Journal of Geotechnical and Geoenvironmental Engineering* 124 (8), 782-
819 787.

820 Ling, H.I., Mohri, Y., Leshchinsky, D., 2005. Large-scale shaking table tests on
821 modular block reinforced Soil retaining walls. *Journal of Geotechnical and*
822 *Geoenvironmental Engineering* 131 (4), 465-476.

823 Matsuo, O., Tsutsumi, T., Yokoyama, K., Saito, Y., 1998. Shaking table tests and
824 analyses of geosynthetic-reinforced soil retaining walls. *Geosynthetics International* 5
825 (1-2), 97-126.

826 Michalowski, R.L., 1998. Limit analysis in stability calculations of reinforced soil
827 structures. *Geotextiles and Geomembranes* 16 (6), 311-331.

828 Michalowski, R.L., You, L., 2000. Displacements of Reinforced Slopes Subjected to
829 Seismic Loads. *Journal of Geotechnical and Geoenvironmental Engineering* 126 (8),
830 685-694.

831 Min, Y., Leshchinsky, D., Ling, H.I., Kaliakin, V.N., 1995. Effects of Sustained and
832 Repeated Tensile Loads on Geogrids Embedded in Sand. *Geotechnical Testing Journal*
833 18 (2), 204-225.

834 Moraci, N., Cardile, G., 2008. Pullout behaviour of different geosynthetics embedded in
835 granular soils, 4th Asian Regional Conference on Geosynthetics, Shanghai, China, pp.
836 146-150.

837 Moraci, N., Cardile, G., 2009. Influence of cyclic tensile loading on pullout resistance
838 of geogrids embedded in a compacted granular soil. *Geotextiles and Geomembranes* 27
839 (6), 475-487.

840 Moraci, N., Cardile, G., 2012. Deformative behaviour of different geogrids embedded
841 in a granular soil under monotonic and cyclic pullout loads. *Geotextiles and*
842 *Geomembranes* 32, 104-110.

843 Moraci, N., Cardile, G., Giofrè, D., Mandaglio, M.C., Calvarano, L.S., Carbone, L.,
844 2014. Soil Geosynthetic Interaction: Design Parameters from Experimental and
845 Theoretical Analysis. *Transportation Infrastructure Geotechnology* 1, 165-227.

846 Moraci, N., Cardile, G., Pisano, M., 2017. Soil-geosynthetic interface behaviour in the
847 anchorage zone [Comportamento all'interfaccia terreno-geosintetico nella zona di
848 ancoraggio]. *Rivista italiana di geotecnica* 51 (1), 5-25.

849 Moraci, N., Recalcati, P., 2006. Factors affecting the pullout behaviour of extruded
850 geogrids embedded in compacted granular soil. *Geotextiles and Geomembranes* 24 (4),
851 220-242.

852 Motta, E., 1996. Earth pressure on reinforced earth walls under general loading. *Soils*
853 *and Foundations* 36 (4), 113-117.

854 Nayeri, A., Fakharian, K., 2009. Study on Pullout Behavior of Uniaxial HDPE Geogrids
855 Under Monotonic and Cyclic Loads. *International Journal of Civil Engineering* 7 (4),
856 211-223.

857 Nernheim, A., 2005. Interaktionsverhalten von Geokunststoff und Erdstoff bei
858 statischen und zyklischen Beanspruchungen. Ph.D. Thesis. TU Clausthal.

859 Newmark, N.M., 1965. Effects of earthquakes on dam and embankments. *Geotechnique*
860 15 (2), 139-160.

861 Nouri, H., Fakher, A., Jones, C.J.F.P., 2006. Development of Horizontal Slice Method
862 for seismic stability analysis of reinforced slopes and walls. *Geotextiles and*
863 *Geomembranes* 24 (3), 175-187.

864 Nova-Roessig, L., Sitar, N., 2006. Centrifuge Model Studies of the Seismic Response of
865 Reinforced Soil Slopes. *Journal of Geotechnical and Geoenvironmental Engineering*
866 132 (3), 388-400.

867 Palmeira, E.M., 2009. Soil–geosynthetic interaction: Modelling and analysis.
868 *Geotextiles and Geomembranes* 27 (5), 368-390.

869 Paulsen, S.B., Kramer, S.L., 2004. A predictive model for seismic displacement of
870 reinforced slopes. *Geosynthetics International* 11 (6), 407-428.

871 Pavanello, P., Carrubba, P., Moraci, N., 2018. Dynamic friction and the seismic
872 performance of geosynthetic interfaces. *Geotextiles and Geomembranes* 46, 715-725.

873 Rahmaninezhad, S., Han, J., Kakrasul, J., Weldu, M., 2019. Stress Distributions and
874 Pullout Responses of Extensible and Inextensible Reinforcement in Soil Using Different
875 Normal Loading Methods. *Geotechnical Testing Journal*.

876 Raju, D.J., Fannin, J., 1997. Monotonic and cyclic pull-out resistance of geogrids.
877 *Geotechnique* 47 (2), 331-337.

878 Razzazan, S., Keshavarz, A., Mosallanezhad, M., 2018. Pullout behavior of polymeric
879 strip in compacted dry granular soil under cyclic tensile load conditions. *Journal of*
880 *Rock Mechanics and Geotechnical Engineering* 10, 968-976.

881 Roodi, G.H., Zornberg, J.G., 2017. Stiffness of Soil-Geosynthetic Composite under
882 Small Displacements. II: Experimental Evaluation. *Journal of Geotechnical and*
883 *Geoenvironmental Engineering* 143.

884 Sabermahani, M., Ghalandarzadeh, A., Fakher, A., 2009. Experimental study on seismic
885 deformation modes of reinforced-soil walls. *Geotextiles and Geomembranes* 27 (2),
886 121-136.

887 Sieira, A.C.C.F., Gerscovich, D.M.S., Sayao, A.S.F.J., 2009. Displacement and load
888 transfer mechanisms of geogrids under pullout condition. *Geotextiles and*
889 *Geomembranes* 27, 241-253.

890 Tatsuoka, F., 2008. Geosynthetics engineering, combining two engineering disciplines,
891 4th Geosynthetics Asia - Special Lecture, Shanghai, Cina, pp. 1-35.

892 Tatsuoka, F., Koseki, J., Tateyama, M., 1995. Performance of geogrid-reinforced soil
893 retaining walls during the Great Hanshin-Awaji Earthquake, January 17, 1995.
894 *Earthquake Geotechnical Engineering Journal*, 55-62.

895 Tatsuoka, F., Koseki, J., Tateyama, M., 1997. Performance of reinforced soil structures
896 during the 1995 Hyogo-ken Nanbu Earthquake. Balkema, Rotterdam, The Netherlands,
897 pp. 973-1008.

898 UNI EN ISO 13286-2, 2010. Miscela non legate e legate con leganti idraulici – Parte 2:
899 Metodi di prova per la determinazione della massa unica e del contenuto di acqua di

900 riferimento di laboratorio – Costipamento Proctor. Ente Nazionale Italiano di
901 Unificazione, Milano.

902 UNI EN ISO 14688-1, 2018. Indagini e prove geotecniche - Identificazione e
903 classificazione dei terreni - Parte 1: Identificazione e descrizione. Ente Nazionale
904 Italiano di Unificazione, Milano.

905 Vieira, C.S., Lopes, M.d.L., 2013. Effects of the loading rate and cyclic loading on the
906 strength and deformation properties of a geosynthetic. *Construction and Building*
907 *Materials* 49, 758-765.

908 Wang, Z., Jacobs, F., Ziegler, M., 2016. Experimental and DEM investigation of
909 geogrid–soil interaction under pullout loads. *Geotextiles and Geomembranes* 44, 230-
910 246.

911 Wartman, J., Rondinel-Oviedo, E.A., Rodriguez-Marek, A., 2006. Performance and
912 Analyses of Mechanically Stabilized Earth Walls in the Tecomán, Mexico Earthquake.
913 *Journal of Performance of Constructed Facilities* 20, 287-299.

914 Watanabe, K., Munaf, Y., Koseki, J., Tateyama, M., Kojima, K., 2003. Behaviors Of
915 Several Types Of Model Retaining Walls Subjected To Irregular Excitation. *Soils And*
916 *Foundations* 43 (5), 13-27.

917 White, D.M., Holtz, R.D., 1994. Performance of Geosynthetic-Reinforced Slopes and
918 Walls During the Northridge, California Earthquake of January 17, 1994, *Earth*
919 *Reinforcement: Proceedings of the International Symposium on Earth Reinforcement,*
920 *IS-Kyushu '96. , Fukuoka, Kyushu, Japan, pp. 965-972.*

- 921 Yasuda, S., Nagase, H., Marui, H., 1992. Cyclic pull-out test of geogrids in soils,
922 International Symposium on Earth Reinforcement Practice, Fukuoka, Japan pp. 185-
923 190.
- 924 Zhou, J., Chen, J.-F., Xue, J.-F., Wang, J.-Q., 2012. Micro-mechanism of the interaction
925 between sand and geogrid transverse ribs. *Geosynthetics International* 19 (6), 426-437.
- 926 Ziegler, M., Timmers, V., 2004. A new approach to design geogrid reinforcement, 3rd
927 European Geosynthetics Conference, Munich, Germany.
- 928